Selective adsorption of organic dyes from aqueous environment using fermented maize extract-enhanced graphene oxide-durian shell derived activated carbon composite

Selective adsorption of organic dyes from aqueous environment using fermented maize extract-enhanced graphene oxide-derived durian shell activated carbon composite

Kehinde Shola Obayomi [a, c*], Sie Yon Lau [a], Michael K. Danquah [b], Jianhua Zhang [c], Tung Chiong [a], Louise Meunier [d], Mohammad Mahmudur Rahman [e, f]

[a] Department of Chemical Engineering, Curtin University, CDT 250, 98009 Miri, Sarawak, Malaysia

[b] Department of Chemical Engineering, University of Tennessee, Chattanooga 615 McCallie Ave, Chattanooga, TN 37403, United States

[c] Institute for Sustainable Industries and Liveable Cities, Victoria University, Werribee, VIC 3030, Australia

[d] Department of Chemical Engineering, Queen's University, Kingston, K7L 3N6, Canada

[e] Global Centre for Environmental Remediation (GCER), College of Engineering, Science and Environment, The University of Newcastle, Callaghan, NSW 2308, Australia

[f] Department of General Educational Development, Faculty of Science and Information, Technology, Daffodil International University, Ashulia, Savar, Dhaka - 1207, Bangladesh

*Corresponding Author

Tel.: +61477318139

E-mail: obayomikehindeshola@gmail.com

Full postal address: Department of Chemical Engineering, Curtin University Malaysia, CDT 250, 98009 Miri, Sarawak.

Institute for Sustainable Industries and Liveable Cities, Victoria University, Werribee, VIC 3030, Australia.

Abstract

A secure aquatic environment is essential for both aquatic and terrestrial life. However, rising populations and the industrial revolution have had a significant impact on the quality of the water environment. Despite the implementation of strong and adapted environmental policies for water treatment worldwide, the issue of organic dyes in wastewater remains challenging. Thus, this study aimed to develop an efficient, cost-effective, and sustainable material to treat methylene blue (MB) in an aqueous environment. In this research, maize extract solution (MES) was utilized as a green cross-linker to induce precipitation, conjugation, and enhance the adsorption performance of graphene oxide (GO) cross-linked with durian shell activated carbon (DSAC), resulting in the formation of a GO@DSAC composite. The composite was investigated for capability to selectively adsorb methylene blue (MB) in aqueous solutions. Physicochemical characterization demonstrated that the cross-linking method significantly influenced the porous structure and surface chemistry of GO@DSAC. BET analysis revealed that the GO@DSAC exhibited dominant mesopores with a surface area of 803.67 m^2/g. EDX and XPS measurements confirmed the successful cross-linking of GO with DSAC. The adsorption experiments were well described by the Harkin-Jura model and they followed pseudo-second order kinetics. The maximum adsorption capacity reached 666.67 mg/g at 318 K. Thermodynamic evaluation indicated a spontaneous, feasible, and endothermic in nature. Regenerability and reusability investigations demonstrated that the GO@DSAC composite could be reused for up to 10 desorption-adsorption cycles with a removal efficiency of 81.78%. The selective adsorptive performance of GO@DSAC was examined in a binary system containing Rhodamine B (RhB) and methylene orange (MO). The results showed a separation efficiency (α) of 98.89% for MB/MO and 93.66% for MB/RhB mixtures, underscoring outstanding separation capabilities of the GO@DSAC composite. Overall, the GO@DSAC composite displayed promising potential for the effective removal of cationic dyes from wastewater.

Keywords: Wastewater treatment; Organic dyes; Adsorption; Graphene oxide; Composite material; Statistical modelling.

1. Introduction

Recently, the contamination of water bodies has become a worldwide concern (Ahmadian et al., 2023). Rapid industrial development, population growth, urbanization, and agricultural activities have significantly contributed to the escalation of water pollution (Cao et al., 2023). Organic dyes, extensively used in industries such as textiles, paper, pharmaceuticals, paints, plastics, leather, cosmetics, tanneries, pigments, and inks, are a major source of pollution (Mu

et al., 2023; Jiang et al., 2023). These water-soluble dyes pose serious threats to the ecological environment due to their mutagenic, carcinogenic, toxic, and non-biodegradable nature (Karmakar et al., 2023). Therefore, it is crucial to develop sustainable, efficient, and cost-effective technologies for treating organic dye-contaminated water bodies, ensuring the preservation and protection of the ecological system and water resources.

Numerous research studies have explored various technologies for organic dye treatment in wastewater, including advanced oxidation, coagulation and flocculation, reverse osmosis, photocatalytic degradation, ion-exchange, filtration, and membrane technology (Wang et al., 2020; Ihaddaden et al., 2022; Saini et al., 2023; Rajesh et al., 2023; Sinha et al., 2021; David et al., 2020; Yan et al., 2021). However, these methods present specific advantages and drawbacks, such as high operating costs, by-product formation, complex operation, and low adsorption capacity (Pandey et al., 2023). Among these methods, adsorption-based treatment has gained significant attention due to its simplicity, high removal efficiency, environmental friendliness, cost-effectiveness, energy-saving properties, regenerability, and reusability (Bhagat et al., 2023; Brandão et al., 2023). However, the success of adsorption treatment relies on the use of efficient adsorbent materials with readily available, abundant surface functionalities, well-developed porous structures, and a high specific surface area. Although various adsorbent materials have been studied, there is a need to develop a novel adsorbent with high selective adsorptive behavior, outstanding adsorption performance, and rapid kinetics (Thakkar et al., 2023).

Graphene oxide (GO) is an effective and attractive adsorbent for wastewater treatment due to its desirable physical and chemical properties, such as thermal stability, tunable structure, exceptional adsorptive ability, high surface area, and high electron mobility (Rajendiran et al., 2022). The presence of surface functionalities, such as epoxy, hydroxyl, and carboxyl groups, allows GO to interact with cationic dyes through chelation or electrostatic interaction (Moradi et al., 2022). However, GO has an edge-to-center distribution of hydrophilic and hydrophobic domains due to the presence of oxidized groups and an unoxidized graphitic lattice, respectively. In addition, it is susceptible to agglomeration in water, which decreases its surface area and reduces its ability to remove pollutants due to strong stacking interactions (Adel et al., 2022; Obayomi et al., 2023a). Therefore, its separation from wastewater after the adsorption of pollutants may be difficult and costly. To overcome these challenges, surface modification of GO with other adsorbent materials is recommended to prevent particle agglomeration, improve adsorptive capacity, and enhance separation and recovery (Jiang et al., 2023).

Activated carbon (AC) is widely recognized as a promising adsorbent for organic and inorganic dyes in aqueous solutions due to its favorable surface area-to-volume ratio, chemical stability, well-developed porous structure, non-toxicity, durability, and excellent adsorptive performance (Goswami and Dey, 2022; Obayomi et al., 2022). The two main approaches for AC preparation are high-temperature carbonization and physical or chemical modification of biochar (Joshiba et al., 2022). However, commercial activated carbon derived from non-sustainable and costly materials like coal is considered expensive (Gul et al., 2022; Tokula et al., 2023). Therefore, there is a need to develop low-cost alternative adsorbents with comparable adsorption capacities to commercial AC to meet global demand and enhance dye removal efficiency (Yadav et al., 2022). Durian shell (Durio zibethinus), an abundant agricultural by-product, has gained attention as a potential raw material for AC production, given its large quantities and availability worldwide. It is estimated that approximately 600,000 metric tons of durian are produced annually, resulting in around 350,000 metric tons of shell waste (Chandra et al., 2007). To avoid environmental pollution caused by the direct disposal of this waste, the development of AC using discarded durian shells has become imperative (Liu et al., 2023).

In order to enhance the adsorptive performance of GO and expand its application in wastewater remediation, a surface modification approach was employed to develop a GO-based composite. While various modification methods have been reported, some involve the use of hazardous, complex, and expensive materials (Abd-Elhamid et al., 2019). However, in order to overcome these challenges, this study aimed to employ fermented maize extract solution (MES) as a cross-linker to induce the precipitation and conjugation between GO and AC. The use of MES demonstrates the benefits of no by-product generation, easy separation, rapid preparation, and reduced GO loss. Maize grain contains proteins, minerals (magnesium, potassium, sodium, and calcium), and carbohydrates (glucose, amylopectin, and amylase). Recent research by Xu et al. (2018) suggested that the presence of sulphur groups (-SH), which can transform into -S-S bonds during thermal treatment, could facilitate stronger cross-linkage with functional groups such as carboxyl, hydroxyl, and epoxide groups present in GO and AC (Ndagijimana et al., 2021). Additionally, the polysaccharides, starch, and proteins in maize grain have gelatinizing properties, making them suitable as gelling agents.

This study prepared a novel and effective durian-derived activated carbon (DSAC) and GO composite using fermented maize grain extract solution (MES) as a cross-linker. The aim was to develop a sustainable and environmentally friendly adsorbent for the selective adsorption of cationic methylene blue (MB) from aqueous solutions, which, to the best of our knowledge,

has not been reported previously. The objectives of the present study were to, (i) prepare GO@DSAC using a sustainable, cost-effective, and eco-friendly technique; (ii) investigate the influence of adsorption variables such as pH, initial MB concentration, temperature, contact time, adsorbent dosage, and competing ions on the adsorptive behavior of GO@DSAC towards MB; (iii) fit the adsorption equilibrium data to adsorption kinetics and isotherm models; (iv) examine the selective adsorption performance of GO@DSAC in a binary mixture; (v) study the regenerability and reusability of the composite through multiple cycles and propose the plausible adsorption mechanism governing the process; and (vi) statistically model the adsorption process using selected variables (pH, temperature) based on the response surface methodology-central composite design (RSM-CCD) approach.

2. Materials and methods

2.1 Materials

Analytical-grade chemicals, including hydrochloric acid (HCl, 37.0%), graphite (99.0%), potassium hydroxide (KOH, 99.9%), hydrogen peroxide (H_2O_2, 30.0%), methylene blue (MB, 99.9%), sulfuric acid (H_2SO_4, 98.0%), sodium nitrate ($NaNO_3$, 99.0%), and potassium permanganate ($KMnO_4$, 99.0%), were obtained from Merck Chemicals and Sigma-Aldrich, Malaysia. The durian shells and maize grain were procured from e-mart in Miri, Malaysia.

2.1 Synthesis of graphene oxide (GO)

Graphene oxide was synthesized using Hummer's method. Two grams of powdered graphite, one gram of $NaNO_3$, and 50 mL of H_2SO_4 were measured and transferred into a 500-mL beaker. The beaker was placed in an ice bath and continuously stirred using a magnetic stirrer for one hour. Then, 15 g of $KMnO_4$ was gradually added at 15 min intervals to maintain the temperature of the mixture below 10 °C. The ice bath was then removed, and the mixture was heated at 35 °C overnight while stirring. After the reaction, 100 mL of deionized water was added drop by drop, and the mixture was heated to 98 °C for 45 min. Next, 20 mL of H_2O_2 was added, and the mixture was stirred for an additional 3 h at room temperature. The resulting brown solution was centrifuged at 3000 rpm for 15 min and washed (using a 5% HCl solution and deionized water). The mixture was then filtered, dried at 60°C overnight in an oven, and finally stored in a sealed container.

2.2 Durian shell activated carbon preparation (DSAC)

Briefly, the durian shells were sliced into smaller sizes, thoroughly washed to remove dirt, and dried in an oven at 105 °C for 18 h. Then, 30 g of the dried durian shell was measured into crucibles and heated in a muffle furnace at a rate of 15 °C/min, reaching a temperature of 550 °C. The process was carried out under flowing nitrogen gas (10 mL/min) for 1 h. Subsequently,

the biochar obtained was impregnated with KOH in a 1:2 (char/KOH) ratio. The mixture was left overnight at room temperature and then washed with 1 M HCl and deionized water to achieve a neutral pH range of 6.7-7.0. Finally, the activated biochar, now referred to as durian shell activated carbon (DSAC), was dried at 80 °C for 24 h and stored in a sealed container for future use.

2.3 Fabrication of GO cross-linked DSAC (GO@DSAC)

First, 10 g of maize grains were winnowed, washed and soaked in a 100 mL of distilled water. The grains were fermented for 3 d. Then, the grains were collected, crushed, and the extract solution (MES) was obtained by sieving through a muslin cloth. Next, 2 g of GO was dispersed in 50 mL of deionized water in a 100 mL beaker using ultrasonication for 30 min. The mixture was then stirred on a magnetic stirrer at 70 °C for 30 min. Afterwards, 4 g of DSAC was added to the mixture under continuous stirring for another 20 min. Subsequently, 3 mL of MES was slowly added to the solution and allowed to stir for an additional 30 min. Once the reaction was complete, the mixture was left for 2 h, and the resulting black precipitate (GO@DSAC) was washed with deionized water. The GO@DSAC was then dried at 80°C for 12 h and thermally treated at 350 °C for 1 h. Finally, it was stored in an airtight plastic bag for further use.

2.4 Material characterization

The GO@DSAC composite was characterized to examine surface charge, surface functional groups, crystallinity, textural morphology, thermal stability, elemental composition, and the atomic electronic state of the material. The elemental composition and morphological structure were examined using a scanning electron microscope (SEM) equipped with an energy-dispersive X-ray analyzer (SEM-EDS, QUANTA 450 FEG D9844, FEI) and an Xplore EDS detector with AztecLiveLiteL software (Oxford Instruments, UK). The functional groups of the material were determined using Fourier-transform infrared spectroscopy (FTIR, Agilent Cary 660). The surface area and porosity of the material were measured using a Brunauer-Emmett-Teller analyzer (BET, TriStar II 3020, Micromeritics) at 77.36 K. The material's surface charge was investigated using a Zeta potentiometer (NanoPlus-3 HD, Zeta Potential and Nano Particle Analyzer, Micromeritics). Insights into the material's crystallinity properties were assessed using powder X-ray diffraction (PXRD, AXS D8 Advance, Bruker, Billerica, MA, USA) with Cu Kα radiation (Kα = 1.541 Å). The material's thermal stability was determined under a N2 atmosphere with a thermogravimetric analyzer (TGA, Pyris 1 model, PerkinElmer, Waltham, MA, USA) using a heating rate of 10 °C/min over a temperature range of 25–1000 °C. The chemical structure and atomic electronic state of the material were examined using X-ray photoelectron spectroscopy (XPS, Mg Kα (1253.6 eV), Kratos Axis

Ultra DLD, UK). The material's size distribution and surface topography were investigated using a high-resolution transmission electron microscope (HRTEM, JEM-2100F, Japan) and atomic force microscopy (Cypher AFM, Oxford Instruments, UK).

2.5 MB adsorption study

A batch adsorption test was conducted in this study to investigate the adsorptive performance of GO@DSAC towards MB. In brief, 50 mg of GO@DSAC was placed in a 250-mL beaker containing 100 mL of various MB concentrations (10-50 mg/L). Then, the mixture was placed on an isothermal shaker at a shaking speed of 600 rpm. The impact of contact time (0-180 min), pH (2-11), adsorbent dosage (0.1-0.6 g/L), and temperature (298-328 K) on the sorption efficiency of GO@DSAC towards MB was examined. Prior to reaching equilibrium, samples were drawn at different time intervals, filtered using a 0.45 μm Millipore filter, and MB residual concentrations were measured at 664 nm using a UV-VIS spectrophotometer (Shimadzu UV-1601 spectrophotometer, Japan). The percentage removal of MB (%) and the adsorption capacity (mg/g) were calculated using Equations 1 and 2, respectively.

$$\%\ MB\ removal = \left(\frac{C_o - C_f}{C_o}\right) \times 100 \quad (1)$$

$$q_e = \frac{(C_0 - C_e) \times V}{W} \quad (2)$$

where C_o, C_f, and C_e represent the initial, final and equilibrium concentrations of MB dye in mg/g; V is the dye solution volume (mL); and W represents the mass of the adsorbent (g).

2.6 Adsorption selectivity study

The selective adsorption performance of GO@DSAC towards MB was investigated in a binary mixture containing MB/MO and MB/RhB. 50 mg of GO@DSAC was weighed and transferred into two separate 250-mL beakers, each containing 100 mL of equal concentrations (50 mg/L) of MB/MO and MB/RhB. The mixtures were then placed on an isothermal shaker at a shaking speed of 600 rpm for 60 min. Thereafter, samples were drawn, filtered, and measured to examine the residual MB concentration using a UV-VIS spectrophotometer. The absorbance of MB, MO, and RhB were measured at 664 nm, 463 nm, and 553 nm, respectively.

2.7 Statistical optimization study

Statistical optimization is an approach used to optimize the key operational variables that influence the adsorption process. In this study, a central composite design (CCD) based on response surface methodology (RSM) was employed to determine the optimal conditions for maximum removal of MB. The statistical model also provides insights into the interaction between the selected factors. The modeling and optimization of MB adsorption onto

GO@DSAC were performed using Design-Expert software (version 11.0). Based on the preliminary experimental study, which employed a single-factor approach, it was found that temperature, adsorbent dosage, and pH had a significant impact on MB removal using GO@DSAC. Therefore, these variables were chosen as input variables for the RSM optimization process, while the output variable was the percentage removal of MB. The independent variable was divided into three levels: 2n axial runs (6 points), 2n factorial runs (8 points), and six center runs (6 points), resulting in a total of 20 experimental runs. All experiments were conducted with an initial MB concentration of 50 mg/L for a duration of 60 min. The variables considered and their coded levels are summarized in Table S1. The relationship between the selected input factors and the response (MB removal) was established using a quadratic model represented by Equation 3.

$$y = \beta_o + \sum_{i=1}^{k} \beta_i X_i + \sum_{i=1}^{k} \beta_{ii} X_i^2 + \sum_{i<j} \beta_{ij} X_i X_j \quad (3)$$

where y represents the MB removal efficiency; X_i is the measured factors; (β_0, β_i, β_{ii} and β_{ij}) are the model relations representing the intercept, quadratic, linear, and interaction coefficients, respectively. Analysis of variance (ANOVA) was performed to determine the relevance and adequacy of the postulated model by calculating the values of the regression parameters, including the lack-of-fit, adjusted R^2 and correlation coefficient (R^2). The relevance of the independent variables on the adsorption process was assessed based on the proposed model at 95% confidence level.

3. Results and discussion

3.1 Material characterization

The SEM examination of the GO@DSAC composite (Fig. 1c) revealed a well-developed pore structure with a heterogeneous mesoporous structure, providing abundant adsorption sites for dye molecules (Elabboudi et al., 2023). The incorporation of DSAC with GO through the cross-linking process resulted in a significant morphological change in the GO@DSAC composite, as evident in Fig. 1a and b, compared with GO and DSAC. The EDX analysis of the composite (Fig. 1d) showed the presence of carbon (26.31%), oxygen (71.22%), sulphur (1.66%), and potassium (0.81%). The lower percentage of carbon compared to oxygen suggests the pyrolysis of C-atoms from DSAC and GO, while the higher percentage of oxygen indicates an increase in the C-O bonds of alkoxy, epoxy, and carboxylic groups in GO and DSAC. The presence of sulphur confirms the successful cross-linking of GO and DSAC using the green method (Ndagijimana et al., 2022). Additionally, the presence of potassium can be attributed to the

chemical activation (KOH) of DSAC. The TEM picture of the GO@DSAC composite (Fig. 1e) reveals that the surface of GO had spherical dark spots of DSAC. AFM analysis was conducted under ambient conditions using tapping mode probes with constant amplitude, and the scanning was performed at multiple positions, as shown in Fig. 1f. The surface roughness of the composite (measured using nasoscope image processing software) was computed as follows: average roughness (R_a) = 17.6 nm, root mean square (R_q) = 27.9 nm, bearing area of 13.3 μm and maximum surface roughness (R_m) = 84.9 nm. The R_q-R_a value of 10.3 nm confirms the distribution of DSAC on GO. Furthermore, the surface of GO@DSAC appeared smooth with unevenly distributed aggregated particles dispersed on the surface.

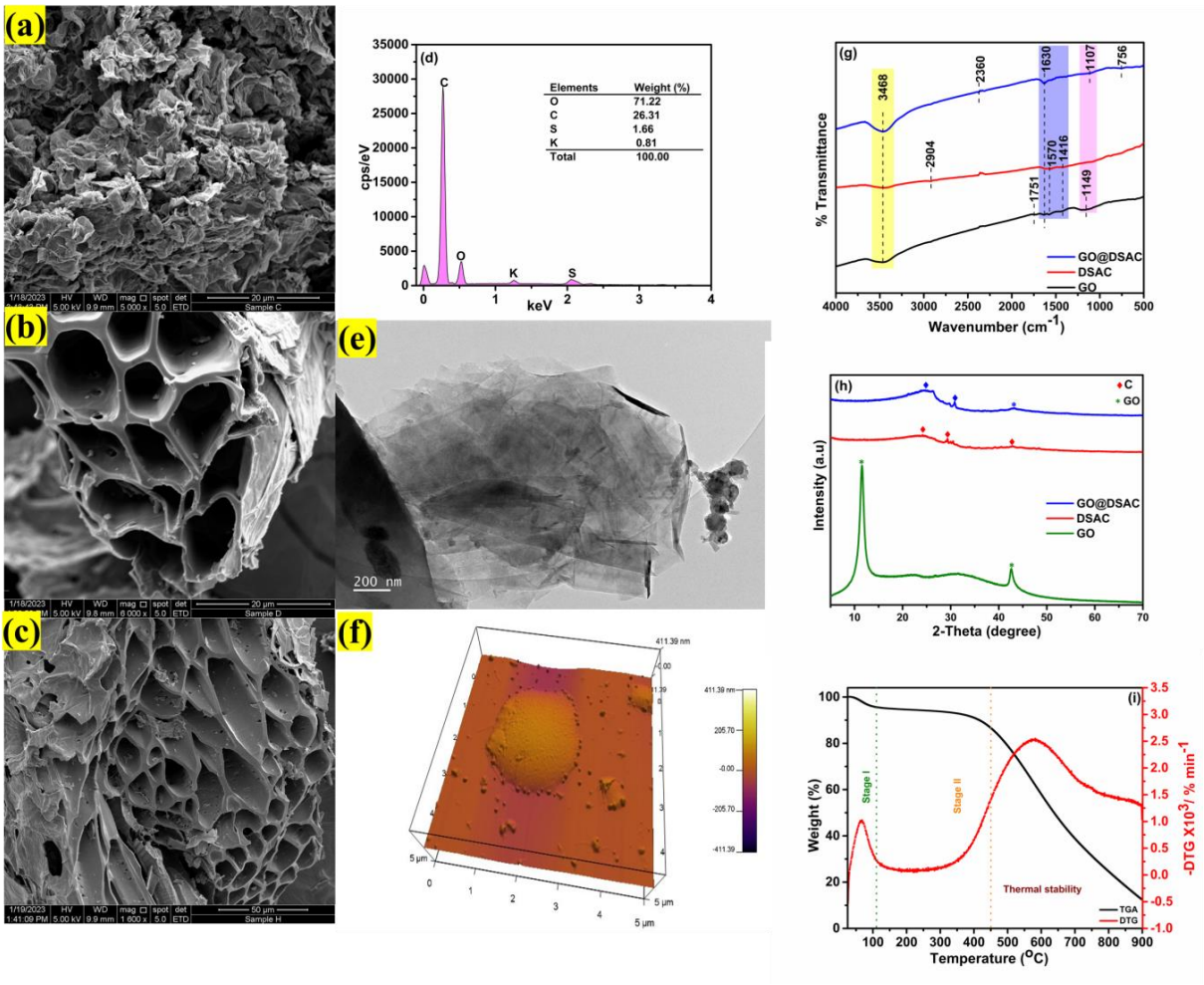

Fig. 1. SEM images of (a) GO, (b) DSAC, and (c) GO@DSAC; EDX analysis of (d) GO@DSAC; TEM/AFM image of (e-f) GO@DSAC; FTIR spectra and XRD pattern of (g-h) GO, DSAC, and GO@DSAC; and TGA/DTG analysis GO@DSAC composite.

The FTIR spectra of GO, DSAC, and the GO@DSAC composite in the wavenumber range between 4000 and 400 cm^{-1} are as presented in Fig. 1(g). The FTIR pattern of GO exhibited a broad peak at 3468 cm^{-1}, which corresponds to the O-H stretching vibration of the hydroxyl group due to adsorbed water molecules (Sajjad et al., 2022). The peak at 1751 cm^{-1} can be attributed to the C=O (-COOH) vibration stretching of the carboxyl group (Rostamian et al.,

2022). The appearance of absorption bands at 1630 and 1570 cm^{-1} indicates C = C stretching vibrations, while the peaks at 1416 and 1149 cm^{-1} correspond to C-OH and C-O of the epoxide group (Babakir et al., 2022). The FTIR spectra of DSAC displayed a broad peak at 3468 cm^{-1}, corresponding to the O-H stretching vibration of the hydroxyl groups found in lignin, cellulose, and hemicellulose. The peaks at 2904 and 1630 cm^{-1} could be attributed to the aliphatic C-H group and C=O stretching vibration of the carboxyl group and hemicellulose, respectively (Jawad et al., 2022). The peaks at 1570 and 1416 cm^{-1} clearly indicate the presence of axial deformation of C=C aromatic lignin and C-OH stretching (Joshiba et al., 2022). The IR spectrum of GO after cross-linking with DSAC (GO@DSAC) using fermented MES revealed peaks at 3468 and 1630 cm^{-1}, suggesting that the O-H group and C=C stretching in the GO and DSAC spectra were retained. The peak at 2904 cm^{-1} in the DSAC spectra, corresponding to the aliphatic C-H group, was reduced to 2360 cm^{-1}. The band at 1149 cm^{-1} in the GO spectra, attributed to the C-O epoxide group, was reduced to 1107 cm^{-1}. The formation of a new peak at 756 cm-1 could be due to C-H bending and the disulphide group (-S-S-), indicating successful cross-linking (Jasri et al., 2023).

The X-ray diffraction pattern of GO, DSAC, and GO@DSAC is as shown in Fig. 1(h). The XRD crystallography pattern of GO exhibited two peaks at 11.6° and 42.8°, assigned to the (001) and (100) crystal planes of the orthorhombic GO phase. This finding suggests that the oxidation of graphite produced the GO phase and introduced oxygen functional groups into the graphite layer (Cahyana et al., 2022). The DSAC diffraction pattern showed three peaks at 24.2°, 29.4°, and 42.8°, respectively. The two primary broad peaks at 24.2° and 42.8°, which can be attributed to the (002) and (100) crystal planes, indicate the graphitization of carbon and the formation of an amorphous structure, which is advantageous for materials with clearly defined pores (Mirzaee et al., 2022; Serafin et al., 2023). The XRD diffraction pattern of the GO@DSAC composite exhibited peaks at 24.2°, 30.8°, and 42.8°. The major peak (002) of DSAC and one of the GO phase peaks (100) were evident in the composite material. However, disappearance of GO crystal phase XRD diffractogram could be attributed to the small amount of GO in the composite, favourable GO dispersion with the matrix and the existence of interfacial interactions. The emergence of GO and DSAC in the composite material demonstrates the successful cross-linking approach for incorporating DSAC into GO (Singh et al., 2022).

The thermal decomposition behavior of GO@DSAC is as presented in Fig. 1(i). The thermograms of GO@DSAC revealed two thermal degradation steps. In the first stage, a weight loss of 4.3% was observed between the temperature ranges of 25-107 °C, which could

be due to the evaporation of adsorbed water and the decomposition of volatile organic matter (Li et al., 2022). The weight loss of 8.93% as the temperature increased from 107 to 450 °C could be attributed to the graphitization of carbonaceous material corresponding to the decomposition of the carboxylic group (Chen et al., 2022). GO@DSAC exhibited high thermal stability between 450-900 °C, which can be attributed to the successful cross-linking of GO with DSAC using MES (Abd-Elhamid et al., 2019). The DTG curve demonstrated that the maximum degradation temperature was experienced at 580 °C.

The BET measurement (Fig. 2a-c) showed that the BET surface areas of GO, DSAC, and GO@DSAC were 82.41, 698.23, and 803.67 cm^2/g, respectively, with average pore volumes of 0.0303, 0.165, and 0.216 cm^3/g, and pore diameters of 3.48, 5.88, and 5.73 nm, respectively. The N2 adsorption-desorption isotherm curves exhibited a type IV behavior, as described by the IUPAC classification. Moreover, based on pore classification, the GO, DSAC, and GO@DSAC composites are dominated by mesopores (2-50 nm). Furthermore, the enhanced surface area of GO@DSAC could be attributed to the cross-linking of GO and DSAC and the disappearance of volatile carbon mass from the composite surface during thermal treatment, thereby providing more pore volume and pore diameter (Saghir et al., 2022).

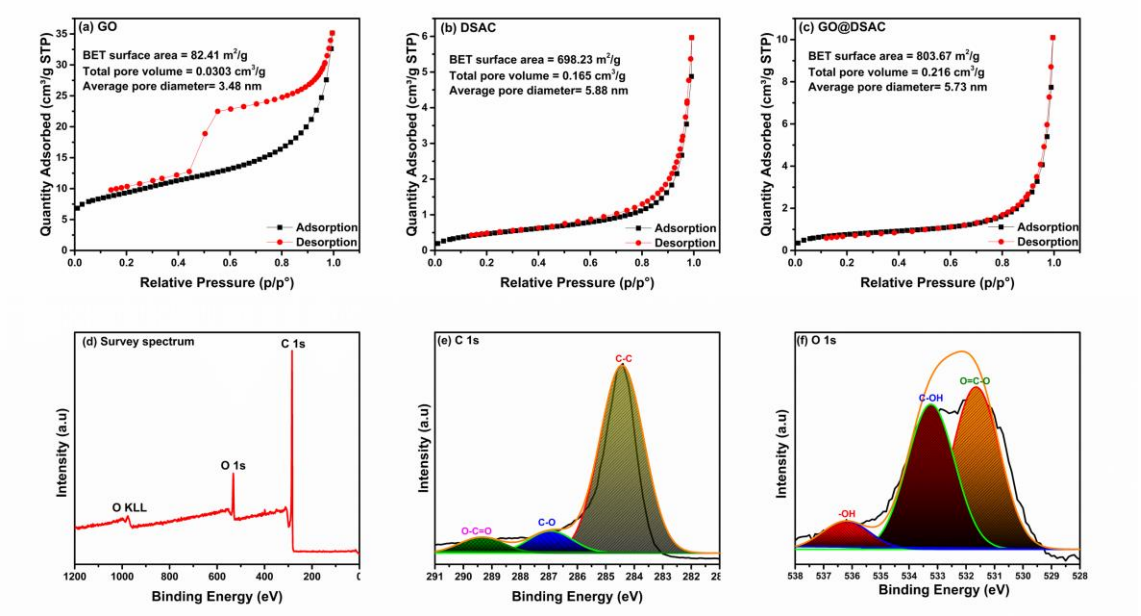

Fig. 2. BET measurement of (a) GO, (b) DSAC, and (c) GO@DSAC and XPS analysis of GO@DSAC for (d) survey spectra, and high-resolution spectra for (e) C 1s, and (f) O 1s.

The XPS survey spectra of the GO@DSAC composite (Fig. 2d) revealed the presence of mainly carbon and oxygen (Mwizerwa et al., 2022). The high-resolution C 1s spectra (Fig. 2e) exhibited three peaks located at 284.4, 286.9, and 289.2 eV. The peak at 284.4 eV is due to C-C bonding (sp^2), the peak at 286.9 eV corresponds to carbon atoms bonded to oxygen (C-O), while the peak at 289.2 eV is assigned to O-C=O (Harraz et al., 2022). The peak at 284.4 eV

clearly indicates the hybridization of the majority of the C-atoms, suggesting the presence of hybridized sp^2 carbon atoms. The peaks at 286.9 and 289.2 eV are due to C-O and O-C=O, indicating the presence of oxygen-related functional groups on the edges and surface of GO@DSAC (Thombare et al., 2022). The high-resolution spectra of O 1s (Fig. 2f) showed peaks at 531.6, 533.2, and 536.2 eV. The peak at 531.6 eV is attributed to O=C-O, relating to the carboxyl groups (COOH). The peak at 533.2 eV is associated with the hydroxyl groups (C-OH), and the peak near 536.2 eV is attributed to weakly bound oxygen resulting from the adsorption of water on the surface of GO@DSAC (Chandraraj and Xavier, 2023).

3.2 Adsorption performance study

The impact of contact time was investigated over a varied time range of 0-180 min at a constant temperature (318 K), pH (8), adsorbent dosage (50 mg), and an initial MB concentration (50 mg/L). The experimental results (Fig. 3a) revealed that the adsorption of MB was rapid within the first 20 min for the different concentrations studied, after which it increased gradually and reached equilibrium at 60 min. However, a slower adsorption rate was observed after equilibrium was established, which could be attributed to the saturation of the majority of sites on the GO@DSAC surface (Xu et al., 2023). Furthermore, it was observed that equilibrium was reached faster at lower MB concentrations compared to higher concentrations. This can be explained by the availability of more adsorption sites on the GO@DSAC composite with fewer MB molecules to occupy them, resulting in a rapid adsorption process at lower concentrations (Han et al., 2023).

The influence of initial MB concentration on the performance capacity and removal efficiency was examined by varying the concentrations from 10 to 50 mg/L while keeping other parameters constant (constant time=60 min, pH=8, adsorbent dosage=50 mg, and temperature=318 K). The results (Fig. 3b) revealed that the MB percentage removal decreased from 96.35% to 80.71% while the performance capacity increased from 118.7 mg/g to 413.7 mg/g with increasing MB concentrations. The decrease in MB efficiency at higher concentrations can be attributed to the saturation of limited adsorption sites, resulting in a queue formation of MB molecules waiting to be adsorbed (Thakkar et al., 2023). Additionally, the adsorption process involves various steps such as the movement of molecules to the external adsorbent surface, diffusion into the adsorbent pores, and further diffusion into the inner pores (Wang et al., 2023; Obayomi et al., 2023b). The increase in adsorption capacity at higher concentrations can be attributed to the competition among more MB molecules present in the solution for the available binding sites on the adsorbent, resulting in a higher adsorption

capacity. Moreover, higher MB concentrations provide more driving force for the diffusion of MB molecules onto the GO@DSAC adsorption sites (Kazak et al., 2023).

The point of zero charge (PZC) of GO@DSAC was measured to determine the adsorbent surface charge. The graph of zeta potential against pH (Fig. 3c) revealed that the PZC of the GO@DSAC composite is 4.69, indicating that the overall GO@DSAC surface is positively charged at pH values below 4.69 and negatively charged at pH values above 4.69 (Yu et al., 2021). Furthermore, the PZC of GO@DSAC increased from 4.69 to 6.51 after MB adsorption, indicating inner sphere complexes (the process at which the MB binds directly to the GO@DSAC surface without the interference of water molecules) and strong electrostatic interaction between GO@DSAC and MB.

The effect of pH on MB adsorption capacity and removal efficiency was investigated by varying the pH between 2 and 11 at the optimum conditions (constant time=60 min, initial MB concentration=50 mg/L; temperature=318 K, and adsorbent dosage= 50 mg) as depicted in Fig.3(d). The positively charged surface of GO@DSAC had low affinity for positively charged MB molecules in acidic conditions due to electrostatic repulsion (Rimzim et al., 2023). Moreover, a higher abundance of positively charged GO@DSAC surface was available at lower pH, resulting in stronger electrostatic repulsion and thus smaller MB removal and adsorption capacity. On the other hand, as the pH exceeded the PZC, the GO@DSAC surface became negatively charged, leading to a stronger affinity for positively charged MB due to electrostatic interaction (Albishri and Katouah, 2023). Furthermore, at higher pH values, the GO@DSAC surface became more negatively charged, resulting in higher MB percentage removal and adsorption capacity. The maximum removal and adsorption capacity, which were found to be 98.82% and 511.7 mg/g, respectively, were achieved at pH 8. Therefore, the adsorption of MB on the GO@DSAC surface is primarily governed by electrostatic interactions.

The effect of GO@DSAC mass was studied by varying the dosage from 0.1 to 0.6 g/L at constant optimum conditions (constant time=60 min, initial MB concentration=50 mg/L; temperature=318 K, and pH= 8). The plot of adsorption capacity and removal efficiency against dosage (Fig. 3e) showed that the percentage MB removal increased with decreasing adsorption capacity as the dosage was increased. The increase in percentage removal can be attributed to the availability of more adsorption sites and the enhanced surface area of GO@DSAC (Demirezen et al., 2023). However, an adsorbent mass increase from 0.1 to 0.3 g/L resulted in 99.01% removal, while further mass increase beyond this point (0.35-0.6 g/L) yielded 96.29%

removal. The decrease in MB removal as the adsorbent mass was further increased could be due to agglomeration on the adsorbent surface, hindering MB molecule adsorption. A significant decline from 126.9 mg/g to 82.3 mg/g was observed in the adsorption capacity of GO@DSAC towards MB with increasing adsorbent mass. This is because at higher adsorbent mass, the number of adsorption sites increases, but at a specified concentration, the adsorption sites are less utilized (Rostamian et al., 2022).

The influence of temperature on the adsorption capacity and removal efficiency of MB onto GO@DSAC was examined to determine the endothermic or exothermic nature of the adsorption process. The plot of adsorption capacity and percentage removal against varying temperature (298-338 K) at optimal conditions (constant time=60 min, initial MB concentration=50 mg/L; pH= 8, and adsorbent dosage 0.3 g/L) is as presented in Fig. 3(f). The results revealed that increasing the reaction temperature led to a significant increase in the adsorption capacity and removal efficiency. For example, by increasing the reaction temperature from 298 to 338 K, the MB removal increased from 88.72% to 98.91%, while the adsorption capacity increased from 113.7 mg/g to 126.6 mg/g. Therefore, the adsorption process of MB onto GO@DSAC was endothermic in nature, and this phenomenon enhanced the interaction between the MB molecules and the active surface of GO@DSAC, providing enough kinetic energy needed for the movement of the MB molecules within the adsorbent surface (Thakkar et al., 2023).

The influence of interfering ions on the adsorptive performance of GO@DSAC towards MB was examined by varying NaCl concentrations ranging from 0 to 0.1% at constant equilibrium conditions (constant time=60 min, initial MB concentration=50 mg/L; temperature=318 K, pH= 8, and adsorbent dosage 0.3 g/L). The results displayed in Fig. 3(g) revealed a significant reduction in the percentage removal and adsorption capacity with increasing NaCl concentration. The drastic decrease in the percentage removal and adsorption capacity can be attributed to the fact that the dissolution of NaCl in the MB solution promotes the formation of Na^+ ions. These ions compete with the positively charged MB molecules for the negatively charged GO@DSAC adsorption sites, thereby leading to a reduction in the percentage removal and adsorption capacity. Furthermore, the presence of salt in the MB solution interferes with the electrostatic interaction between the GO@DSAC surface and the MB molecules.

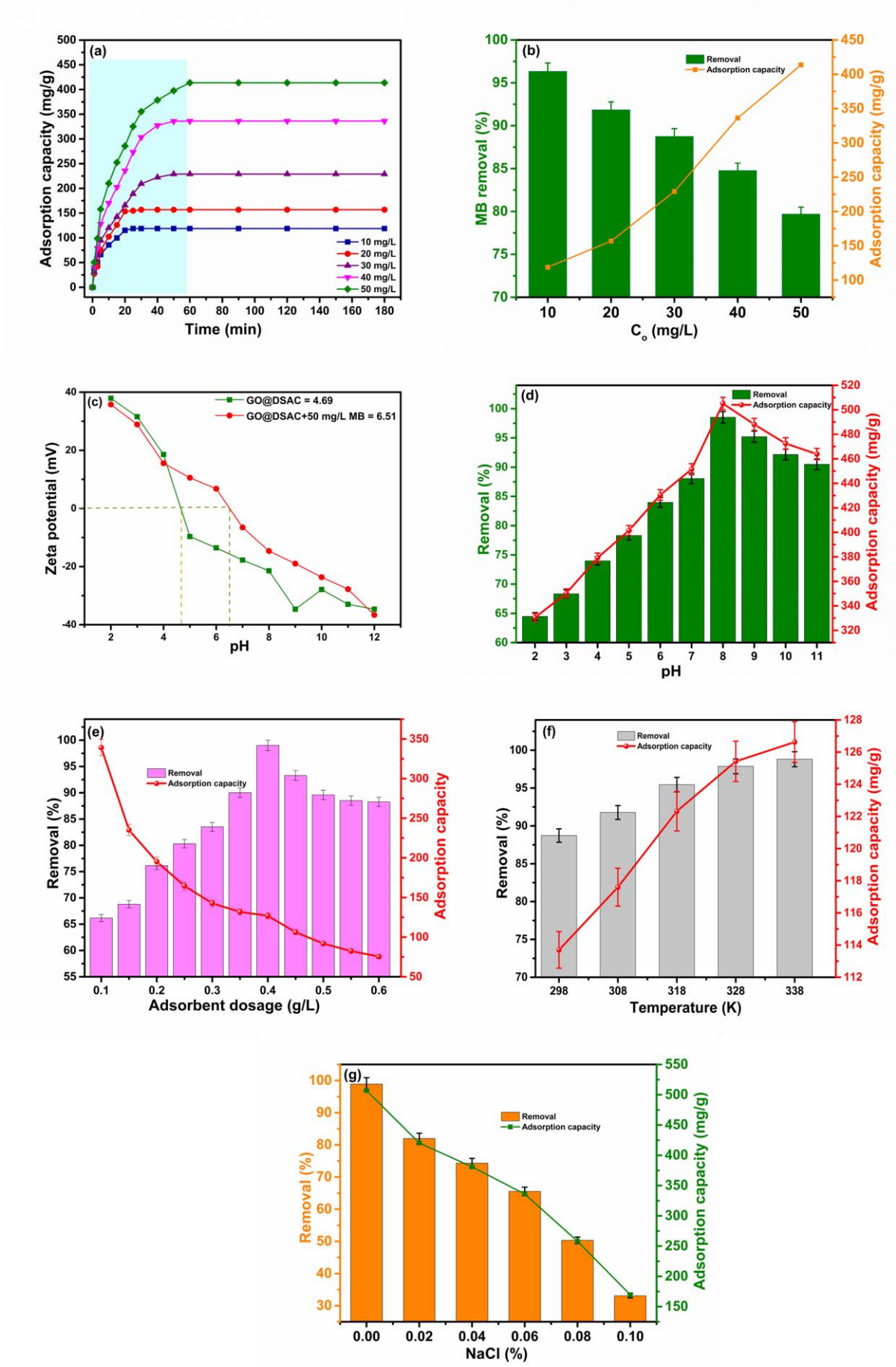

Fig. 3. The plots (a) contact time, (b) initial MB concentration, (c) PZC, (d) adsorbent dosage, (e) temperature, and (f) competing ions on MB removal by GO@DSAC.

3.3 Adsorption isotherm study

The distribution of adsorption molecules between the liquid and solid phases is controlled by the adsorption isotherm in an equilibrium adsorption condition (Jia et al., 2022). Moreover, adsorption equilibrium is reached when, at a fixed temperature, the amount of adsorbate in the liquid and on the surface of the adsorbent is evenly distributed, and no further net adsorption occurs. Although numerous isotherm models have been developed in an effort to fit the experimental data, none of them are precise, and all entail assumptions (Pandey et al., 2022). The experimental data obtained from MB adsorption onto the GO@DSAC composite was fitted to eight different isotherm models: Langmuir, Freundlich, Temkin, Dubinin–Radushkevich, Jovanovic, Harkins-Jura, Halsey, and Redlich-Peterson. The isotherm model fitting equations and curves are shown in Table S2 and Fig. 4(a-h). The model parameters and their corresponding values (Table S3) revealed that the adsorption process of MB onto the GO@DSAC surface was better explained by the Harkins-Jura isotherm (>0.99) model, followed by Jovanovic (<0.99), Halsey (<0.96), Redlich-Peterson (<0.96), Freundlich (<0.96), Temkin (<0.90), Langmuir (<0.84), and Dubinin–Radushkevich (<0.80). This conclusion was based on their high coefficient of correlation (R^2) and smaller Hybrid fractional error function (HYBRID), smaller sum of square errors (SSE) values. The compatibility of the Harkins-Jura model with the adsorption process suggests that MB adsorption onto the GO@DSAC composite is dominated by multilayer adsorption occurring on a heterogeneous surface, and this is also supported by the Freundlich (R^2= 0.951) and Halsey models (R^2= 0.952). The Temkin and Dubinin–Radushkevich models suggest that the adsorption process is physical in nature and occurs as a result of weak van der Waals forces (b_T and E < 8 kJ/mol) (Al-Jubouri et al., 2023).

Furthermore, the maximum adsorption capacities calculated from the Langmuir model were 523.56, 588.23, and 666.67 mg/g at 298, 308, and 318 K, respectively. The high adsorption capacity could be due to the following reasons: first, the GO@DSAC possesses a porous structure and high surface area, which allows the MB molecules to diffuse and access the pore sites of the composite. Secondly, the abundant negatively charged GO@DSAC surface is able to adsorb positively charged cationic MB dye through strong electrostatic interaction (Hou et al., 2023). The maximum adsorption capacity of GO@DSAC towards MB was compared with other adsorbents, and the results are depicted in Table 1. The results revealed that the adsorptive performance of GO@DSAC exhibited a higher adsorption capacity than most adsorbent materials reported in previous studies.

Table 1. Comparison of GO@DSAC adsorption capacity on MB with other adsorbents

Adsorbent	Experimental conditions	Q_m (mg/g)	References
β-CD/GO	pH 7, 343 K, 60 min	76.4	Yang et al., (2021)
GT-CAG-cl-polyAA	720 min, 303 K	312.7	Sharma et al., (2022)
CMC/PAA/GO	pH 9, 250 min, 298 K	138.0	Hosseini et al., (2022)
Fe_3O_4/TiO_2/graphene sponge	pH 9, 10 min, 328 K	224.0	Maimaiti et al., (2022)
CMC/GAs-30	298 K	222.7	Liu et al., (2022)
2Ala-2Car-1GO	pH 9.2, 298 K	132.4	Rather et al., (2022)
MSGO-4	pH 8, 90 min	260.9	Zhu et al., (2023)
PDOP/GO	pH 7, 1440 min, 298 K	270.0	Thu et al., (2023)
GO-PLA	pH 7, 298 K	332.5	Nouri et al., (2023)
ZA/GO	pH 6, 240 min, 298 K	145.1	Jing et al., (2023)
GO@DSAC	pH 8, 60 min, 318 K	666.7	This study

3.4 Adsorption kinetics study

The present study investigated the rate-limiting step during the adsorption process of MB onto GO@DSAC. The experimental data were fitted to the pseudo-first-order, pseudo-second-order, Elovich, intraparticle diffusion, and Boyd models. The model equations and fitting curves are as presented in Table S2 and Fig. 4(i-m). Comparison of the kinetic model parameters based on their R^2 and standard error (SE) values, as depicted in Table S4, revealed that the adsorption behavior of MB on GO@DSAC was better explained by the pseudo-second-order kinetic model due to its high R^2 (>0.997) and smaller SE (<0.004) (Li et al., 2023). Furthermore, the experimental adsorption capacity ($q_{e,\,exp}$) values at different concentrations were closer to the calculated adsorption capacity ($q_{e,\,cal}$) values for the pseudo-second-order model during the experimental study (Du et al., 2023). In addition, the Elovich model adsorption rate constant (α) values calculated at different concentrations were higher than the desorption rate constant (β), suggesting that MB adsorption onto GO@DSAC was higher at the initial stage of adsorption. The intraparticle diffusion plot shown in Fig. 4(l) demonstrated that the adsorption behavior contained three stages, suggesting that the adsorption process was controlled by the boundary layer at the initial stage, followed by slow intraparticle diffusion, and finally, the equilibrium stage. The first stage, which was the fastest, showed that MB molecules moved rapidly into the mesoporous structure of GO@DSAC and occupied the adsorption external sites. During the second stage, the MB molecules diffused slowly through the liquid film into the interior GO@DSAC surface. At the final stage, which was the slowest, the equilibrium position was established as a result of the adsorbent surface saturation caused by adsorbed MB molecules (Shimizu et al., 2022). Furthermore, as observed from the intraparticle diffusion plot, the experimental data fitting did not pass through the origin, indicating that the adsorption behavior was not completely controlled by intraparticle diffusion but that external diffusion might be involved. Furthermore, the Boyd model fitting plot depicted in Fig. 4(m) clearly

demonstrated that the straight line did not pass through the origin, suggesting that both intraparticle diffusion and external mass transfer governed the adsorptive behavior of GO@DSAC towards MB molecules (Al-Jubouri et al., 2023).

Thermodynamics evaluation

The thermodynamic properties of MB adsorption on GO@DSAC composite was investigated using the adsorption isotherm data at different temperatures to reveal the driving force and degree of the adsorption process (Obayomi et al., 2023c).

$$\Delta G = \Delta G^o + RT \ln K^o_{Equilibrium} \quad (4)$$

$$-\Delta G^o = RT \ln K^o_{Equilibrium} \quad (5)$$

$$\Delta G^o = \Delta H^o - T\Delta S^o \quad (6)$$

The Van't Hoff equation is given as;

$$\ln K^o_{Equilibrium} = -\frac{\Delta H^o}{RT} + \frac{\Delta S^o}{R} \quad (7)$$

$$K^o_{Equilibrium} = \frac{(K_L \times M_w \times 1000) \times [C^o]}{\gamma} \quad (8)$$

where $K^o_{Equilibrium}$ is the thermodynamic equilibrium constant (dimensionless), M_w stands for the MB molecular weight (319.85 g/mol), K_L represents the Langmuir constant, K_L (L/mg), γ is the coefficient activity of MB in solution (dimensionless) and [C]° is the standard concentration of the MB (1 mol/L). Since the MB dye solution is very diluted, the activity of coefficient (γ) is considered unitary (Lima et al., 2019). The adsorption activation energy was calculated to further confirm the nature of adsorption during MB with GO@DSAC. The Arrhenius equation is represented by;

$$\ln k_2 = -\frac{E_a}{R}\left(\frac{1}{T}\right) + \ln A \quad (9)$$

Where E_a is adsorption activation energy (kJ/mol), A is the Arrhenius constant, and k_2 is the rate constant for the pseudo-second order. The values of E_a and A were determined from the slope and intercept of the plot of $\ln k_2$ $against$ $\frac{1}{T}$ (plot not shown). Values of E_a between 5-40 kJ/mol suggest physical properties while values between 40-80 kJ/mol reveal chemical properties. The values of ΔS^o and ΔH^o were obtained from the slope and intercept of $\ln K^o_{Equilibrium}$ versus 1/T as shown in Fig. 4(n). The thermodynamics results presented in Table S5 shows that the negative ΔG^o values calculated suggest that the adsorption of MB on GO@DSAC occurs spontaneously and feasibly. Furthermore, the ΔG^o values decrease with increasing temperature, indicating that the adsorption process is more favoured at higher temperature (Ahmad and Ejaz, 2023).

The positive ΔH^o values revealed that the interaction between the MB molecules and GO@DSAC was physical and endothermic in nature. This was also confirmed by ΔH^o and E_a (< 40 kJ/mol) values. The positive ΔS^o values demonstrated an increase in randomness during the adsorption process at the MB-GO@DSAC interface (Wang et al., 2023). Finally, the activation energy during the adsorption of MB on GO@DSAC was 22.122 kJ/mol.

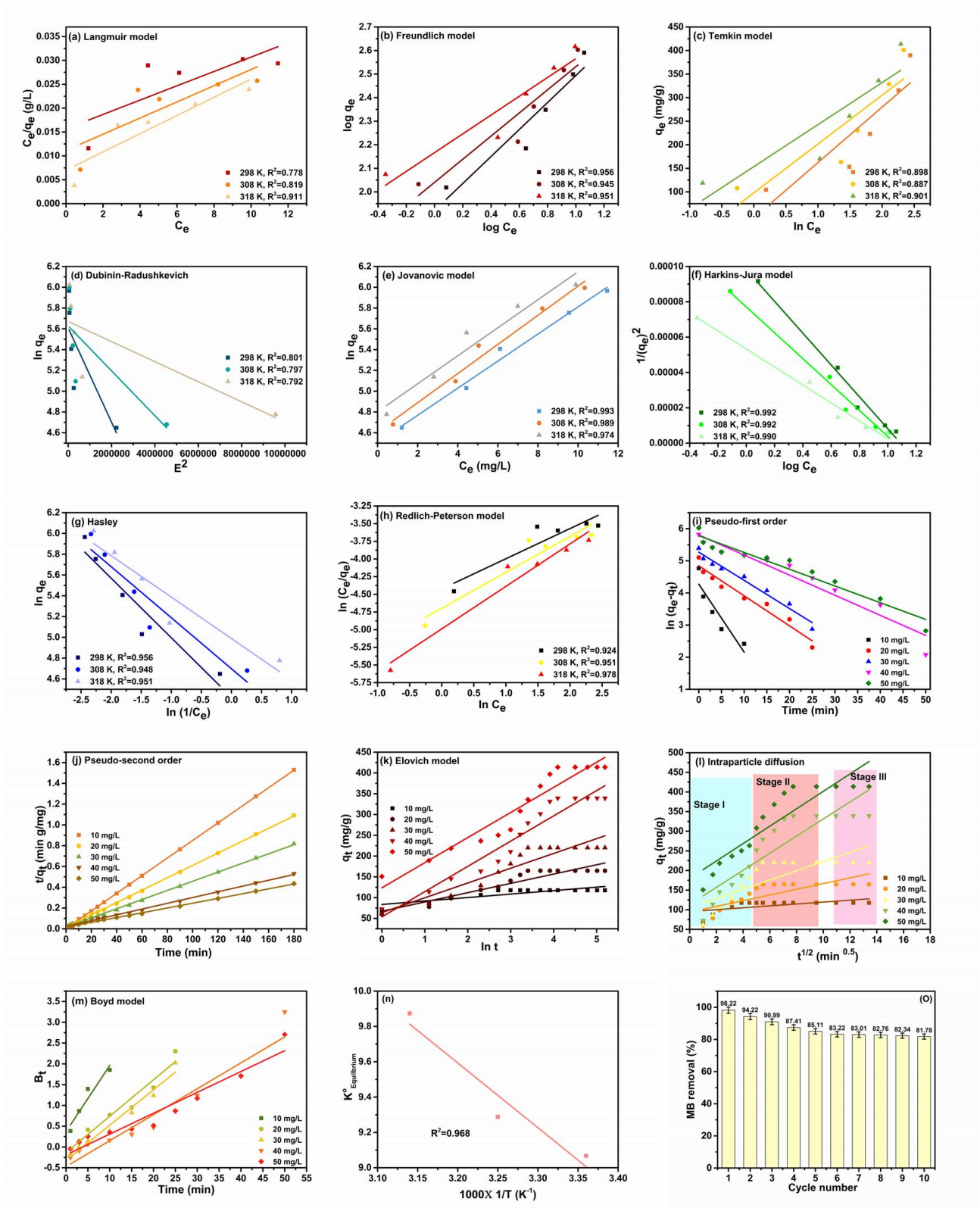

Fig. 4. Adsorption isotherms (a-h), kinetics (i-m), thermodynamics (n), and reuseability study (o) plots for MB adsorption by GO@DSAC.

3.6 Regenerability and reusability study

To explore the reusability of the GO@DSAC composite and achieve sustainable application, a desorption experiment was conducted after the completion of the adsorption process by thoroughly washing the composite with a solution mixture containing 5% acetic acid in ethanol. Acetic acid was used to destroy the electrostatic interaction between MB and GO@DSAC. The composite was then washed with deionized water six times, centrifuged at 3000 rpm for 10 min, and finally dried in an oven at 102°C for 4 h. The adsorption-desorption process was repeated 10 times following the same procedure. The cyclic experimental results (Fig. 4o) revealed that the MB percentage adsorption reached 98.22% in the first cycle and decreased to 81.78% after the tenth cycle. The decrease in the percentage MB removal after each cycle could be due to blockade of pores by unflinching MB molecules thereby reducing the active sites of the GO@DSAC composite. Together, the results suggest that the composite material has good stability and reusability performance, making it a sustainable adsorbent for wastewater treatment.

3.7 Adsorption mechanism

To examine the mechanism governing the interaction between MB molecules and GO@DSAC, pH, BET, XRD, FTIR, AFM, and XPS analyses were performed before and after adsorption. The effect of pH on the adsorptive performance of GO@DSAC towards MB revealed that the electrostatic interaction was the primary mechanism governing the adsorption process. When the pH of the solution was above the PZC (4.69), the adsorption sites on GO@DSAC were positively charged, thereby promoting a strong electrostatic attraction with the cationic MB. BET measurements also demonstrated that the BET surface area and pore volume of GO@DSAC before MB adsorption were 803.67 m^2/g and 0.216 cm^3/g, respectively, while after MB adsorption, they were 489 m^2/g and 0.0998 cm^3/g. The FTIR analysis of the adsorption mechanism between MB and porous GO@DSAC before and after adsorption is as depicted in Fig. 5(a). A shift in the peak assigned to O-H stretching vibration was observed from 3468 cm^{-1} to 3440 cm^{-1}, suggesting hydrogen bonding between MB and GO@DSAC. The peak at 2360 cm^{-1} corresponding to the aliphatic C-H group shifted to 2372 cm^{-1}. This shift was likely a result of surface modification; at pH 8, the hydrogen ions and carbonyl group on the GO@DSAC surface transformed into carboxylic and hydroxylic groups, creating an avenue for the MB molecules to be more easily captured (Zhang et al., 2023). Furthermore, the peaks at 1630 cm^{-1} and 1107 cm^{-1}, relating to C=C stretching and C-O of the epoxide group, were seen to be broader, demonstrating that the surface of GO@DSAC was successfully covered with MB molecules. The XRD diffraction pattern before and after MB adsorption, presented

591 in Fig. 5(b), revealed no observable change in the crystal structure of GO@DSAC (no
592 formation or disappearance of peaks), indicating that the adsorption process involved a physical
593 adsorption mechanism. The SEM analysis depicted in Fig. 5(c) showed that the morphological
594 structure of the material was not damaged but rather the porous surface of the adsorbent was
595 filled with the adsorbed MB, suggesting that the adsorption process involved physical
596 adsorption. Furthermore, the AFM analysis before and after adsorption, presented in Fig. 5(d),
597 showed that the maximum surface roughness of the porous material increased after MB
598 adsorption from 84.88 nm to 101.20 nm, suggesting the successful adsorption of MB
599 molecules. The XPS full spectra of GO@DSAC before and after MB adsorption, depicted in
600 Fig. 5(e), demonstrated the presence of N Is in the GO@DSAC structure after adsorption,
601 confirming that MB adhered to the surface of GO@DSAC. The N 1s deconvolution spectrum
602 depicted in Fig. 5(f) showed three peaks at 400.4 eV, 399.6 eV, and 398.2 eV corresponding
603 to $–NH_3^+$ (protonated amino), C-N-C, and $–NH_2$ (amino) groups. The functional groups were
604 fully involved in the adsorption process of MB on GO@DSAC via electrostatic interaction
605 (Kumari et al., 2020). Finally, based on the aforementioned findings, hydrogen bonding,
606 physical adsorption, pore-filling, and electrostatic interaction might be the major factors
607 governing the interaction between MB and GO@DSAC.

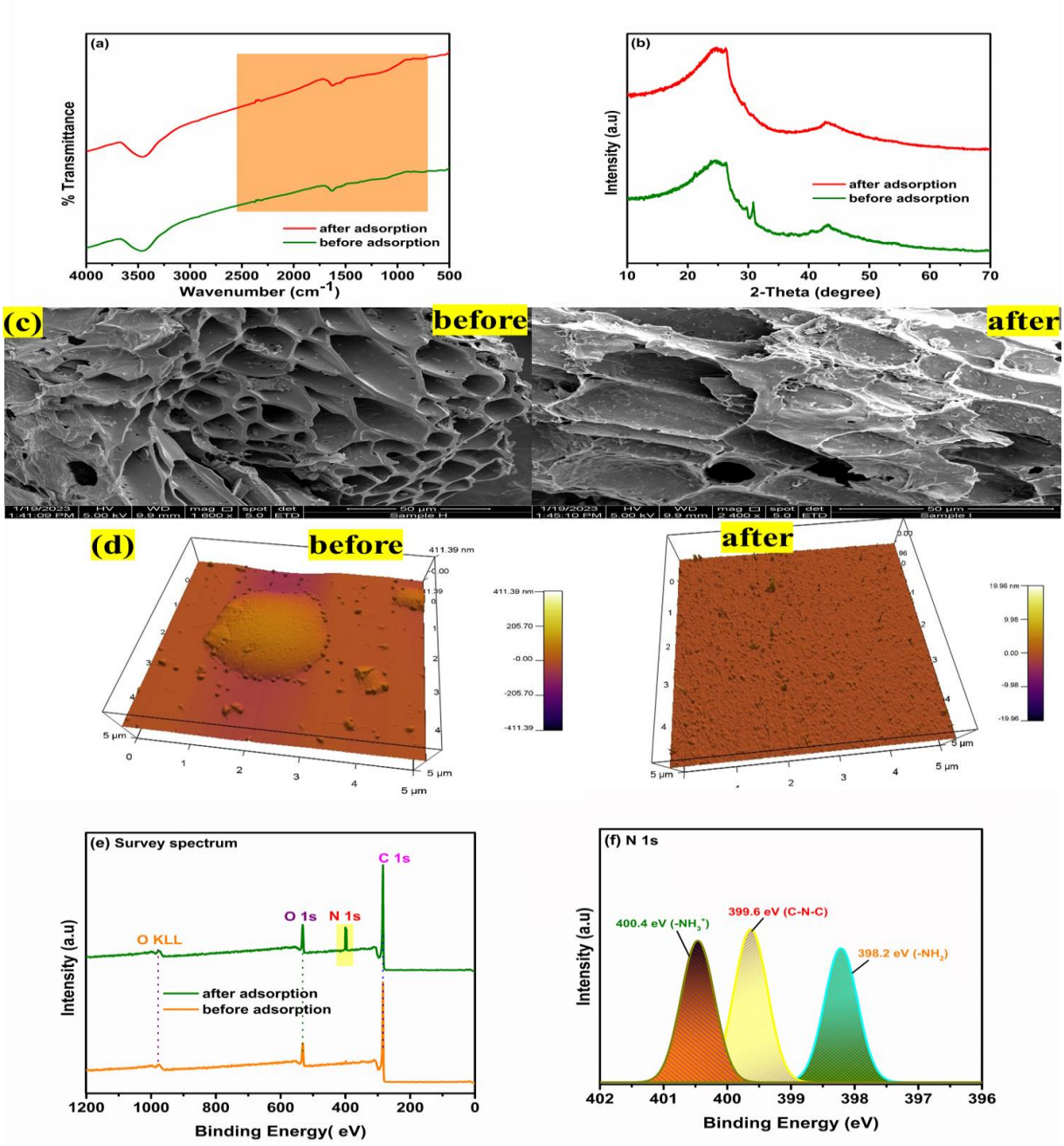

Fig. 5. (a) FTIR, (b) XRD, (c) SEM, (d) AFM, and (e-f) XPS analysis of MB adsorption on GO@DSAC before and after adsorption.

3.7 Selective adsorption study

In practical applications, the performance of an adsorbent material depends on its outstanding adsorptive selectivity for a specific dye from a binary or multiple mixture system. The present study examined the adsorptive performance of GO@DSAC towards cationic dyes (MB and Rhodamine B (RhB)), anionic dye (methylene orange (MO)), and in a binary mixture system (MB/MO and MB/RhB) under optimum conditions of pH 8, adsorbent dosage of 0.3 g/L, initial concentrations of 50 mg/L, temperature of 318 K, and a contact time of 60 min. In the singular component system, the performance of GO@DSAC was tested towards MB, MO, and RhB, as depicted in Fig. 6(a-c). The percentage removal of MB, RhB, and MO was 97.2%, 32.32%,

and 4.62%, respectively. The results suggested that electrostatic attraction and hydrogen bonding might play an important role in the interaction between GO@DSAC and the dyes. The low percentage removal of MO was understandable because at pH 8, the overall surface of the adsorbent was deprotonated, making GO@DSAC negatively charged. This led to electrostatic repulsion with the anionic, negatively charged MO but facilitated electrostatic attraction between the cationic, positively charged MB (Konno and Tsukada, 2020). Furthermore, the percentage removal of 32.32% recorded for RhB could be due to the fact that RhB (pKa = 3.7) ionizes with increasing pH, resulting in the formation of a more negative charge (Meng and Nan et al., 2022). Therefore, as the pH is increased to 8, RhB becomes more negatively charged, enhancing electrostatic repulsion between RhB and GO@DSAC. The color comparison of MB, RhB, and MO before and after adsorption onto GO@DSAC revealed no obvious change in the color of RhB and MO, suggesting that GO@DSAC has a weak affinity for RhB and MO (Kumari et al., 2020).

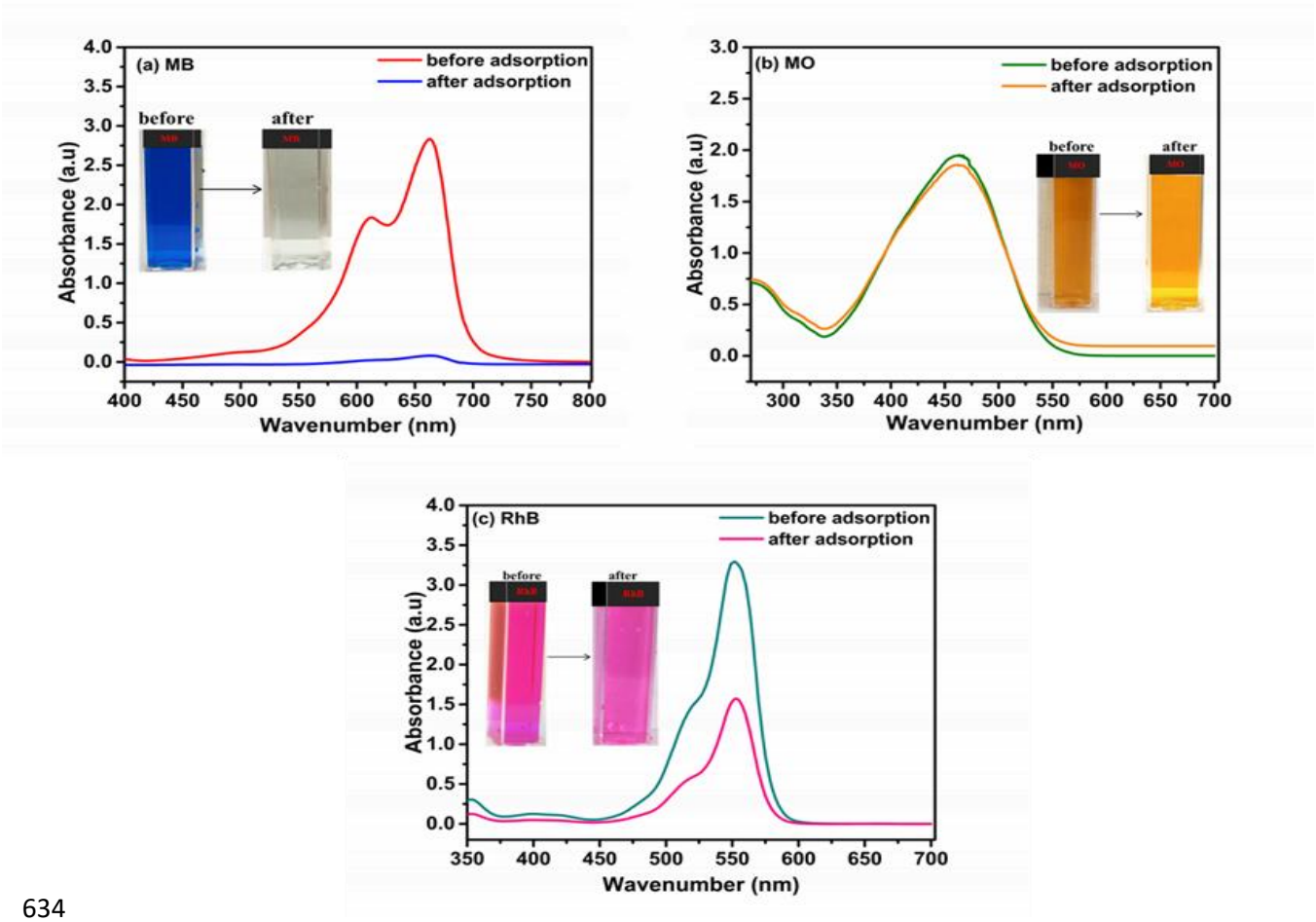

Fig. 6. UV–Vis absorbance spectra and pictorial view of (a) MB (b) MO, and (c) RhB in a singular component before and after adsorption on GO@DSAC.

The adsorptive selectivity of GO@DSAC in a binary mixture (MB/MO and MB/RhB), using MB as the target dye, and RhB or MO as the competing species, was investigated, and the results are presented in Fig. 7(a-d). The pictorial representation of the mixed color before and

after adsorption by GO@DSAC, depicted in Fig. 7(a-b), showed that the color of the binary mixture after adsorption was almost close to that of the MO and RhB solutions. This fact suggests that in the binary dye component, cationic MB was mostly adsorbed by GO@DSAC, confirming that GO@DSAC had higher adsorptive selectivity towards cationic MB. As observed in Fig. 7(c-d), the UV-vis absorbance spectra corresponding to MB were observed to have declined significantly, while the absorbance spectra of RhB and MO decreased slightly after adsorption by GO@DSAC. Furthermore, the separation efficiency ($\propto$) calculated for MB in MB/MO and MB/RhB was 98.89% and 96.66%, respectively. It is evident from the results that the interaction between the dyes and GO@DSAC was primarily governed by electrostatic force (Xu et al., 2023). Therefore, the selective adsorption experiments conducted in a basic medium facilitated the adsorption of cationic MB and repelled the adsorption of RhB and MO onto the GO@DSAC surface (Zhang et al., 2023). Thus, as an efficient adsorbent with outstanding adsorptive selectivity, GO@DSAC has a wide prospect in the treatment of wastewater containing cationic dyes.

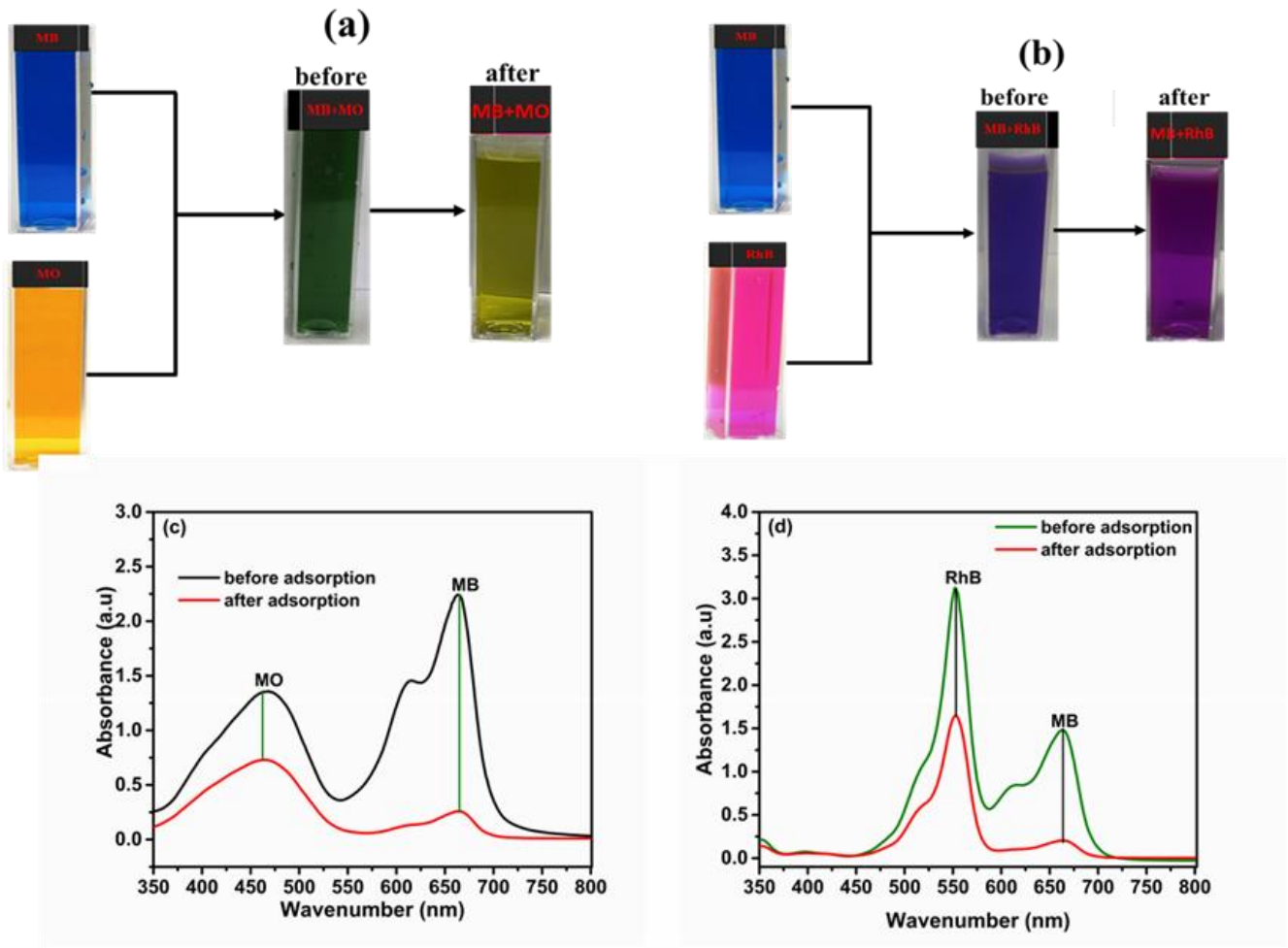

Fig. 7. Pictorial representation (a-b), and UV–Vis absorbance spectra (c-d) for a binary mixture of MB/MO, and MB/RhB before and after adsorption of by GO@DSAC.

3.9 RSM optimization of MB removal

In order to examine the influence of independent variables such as temperature, adsorbent dosage, and pH, as well as their interactive effects on the maximum MB removal on GO@DSAC, a Central Composite Design (CCD), which is an aspect of Response Surface Methodology (RSM) statistical modeling, was employed using the optimal results from the singular variable at a time experimental approach. The results obtained from the 20 experimental runs, as predicted by the CCD, revealed that the minimum and maximum MB removal, as shown in Table S6, were 98.97% and 44.40%, respectively.

Furthermore, the model response (MB removal) using the RSM-CCD modelling was employed to develop a second-order quadratic polynomial model that relates the variables (temperature, adsorbent dosage, pH) to the response (MB removal). The GO@DSAC composite adsorptive behaviour towards MB is expressed using the quadratic regression model:

$$\text{MB removal (\%)} = +91.58 + 5.05\,A - 4.67\,B + 10.72\,C + 2.63\,AB + 1.03\,AC - 3.41\,BC + 2.34\,A^2 - 11.69\,B^2 - 18.68\,C^2 \quad (11)$$

However, the adequacy of the RSM-CCD model was examined using the analysis of variance (ANOVA) test, and the results are presented in Table S7. It was revealed that the quadratic model had an F-value of 354.92 with a P-value of <0.0001 ($p < 0.05$), suggesting that the model was significant, and the lack-of-fit was not significant, which is acceptable. The correlation coefficient (R^2), which measures the model fitness, was 0.997, demonstrating the closeness of the predicted response to the actual response (Sadeghnezhad et al., 2022). The adjusted and predicted R^2 values of 0.994 and 0.981 presented in Table S8 revealed that the model was sufficiently good to predict the adsorption process. The model predicted that temperature, adsorbent dosage, and pH had a significant effect on the adsorption process (p-values < 0.05) in terms of linear, two-factor, and quadratic interaction. The normal plot of residuals based on residuals, externally, and internally studentized residuals (Fig. S1(a-c)) revealed that the points were closer to the straight lines and followed a normal distribution (Boulahbal et al., 2022).

The 3-D response surfaces and 2-D contour plots illustrated in Fig. 8(a-c) were further employed to understand the interaction effect between two independent variables when used simultaneously to predict the optimal conditions for achieving the maximum MB removal. The interactive effect of temperature and adsorbent dosage at a constant pH is presented in Fig. 8(a). An increase in temperature resulted in a significant increase in the percentage removal, while an increase in adsorbent dosage from 0.1 to 0.3 g/L also resulted in higher MB removal but decreased with further increase in adsorbent dosage. However, the maximum MB removal

was achieved at the highest temperature (318 K) and a moderate adsorbent dosage (0.3 g/L). The highest MB removal with increasing temperature could be due to the increase in kinetic energy, which was sufficient to reduce the viscosity of the solution and allow MB molecules to diffuse and move freely on the GO@DSAC surface.

The combined effect of temperature and pH at a constant adsorbent dosage is depicted in Fig. 8(b). The synergetic effect of temperature and pH minimally influenced the removal of MB, as indicated by their small F-value (8.53) in Table S7 compared to other interactive variables. The highest MB removal was achieved with a high temperature and a moderate pH. Specifically, the highest MB removal was observed at a temperature of 318 K and a pH of 8. In an acidic medium, the adsorbent surface was protonated (pH < PZC), resulting in electrostatic repulsion between the cationic MB and the positively charged GO@DSAC. However, as the pH increased (pH > PZC), the composite surface was deprotonated, making the adsorbent surface more negatively charged, which facilitated the adsorption of cationic MB through electrostatic attraction. However, further increases in pH above 8 resulted in a decrease in MB removal, suggesting an oversaturation of the adsorbent adsorption sites by MB molecules.

The impact of pH and adsorbent dosage at a constant temperature is depicted in Fig. 8(c). The 3-D and contour plots show that the effect of pH and adsorbent dosage had the most significant impact on MB removal, which is confirmed by their highest F-value (93.16) as shown in Table S7. Increasing the pH from 2 to 8 and the adsorbent dosage from 0.1 to 0.3 g/L resulted in the highest MB removal. The maximum MB removal was achieved at pH 8 and an adsorbent dosage of 0.3 g/L. However, increasing the adsorbent dosage (>0.3 g/L) and pH (>8) beyond this point resulted in a decrease in MB removal. This decline may be due to adsorption site blockage resulting from particle agglomeration on the adsorbent surface as the adsorbent dosage increases.

The main goal of the statistical analysis was to model optimal conditions for maximum MB removal efficiency during the adsorption process using numerical optimization. Based on the desirability of the model (1.0), the selected optimal conditions of temperature = 316.17 K, adsorbent dosage = 0.26 g/L, and pH = 9.13 resulted in a removal efficiency of 98.41%. A confirmatory test was then performed to further validate the predicted MB removal using the selected optimal variables. The experimental and predicted results obtained for MB removal were 98.97% and 98.41%, respectively, suggesting a good a close agreement between the predicted and experimental values.

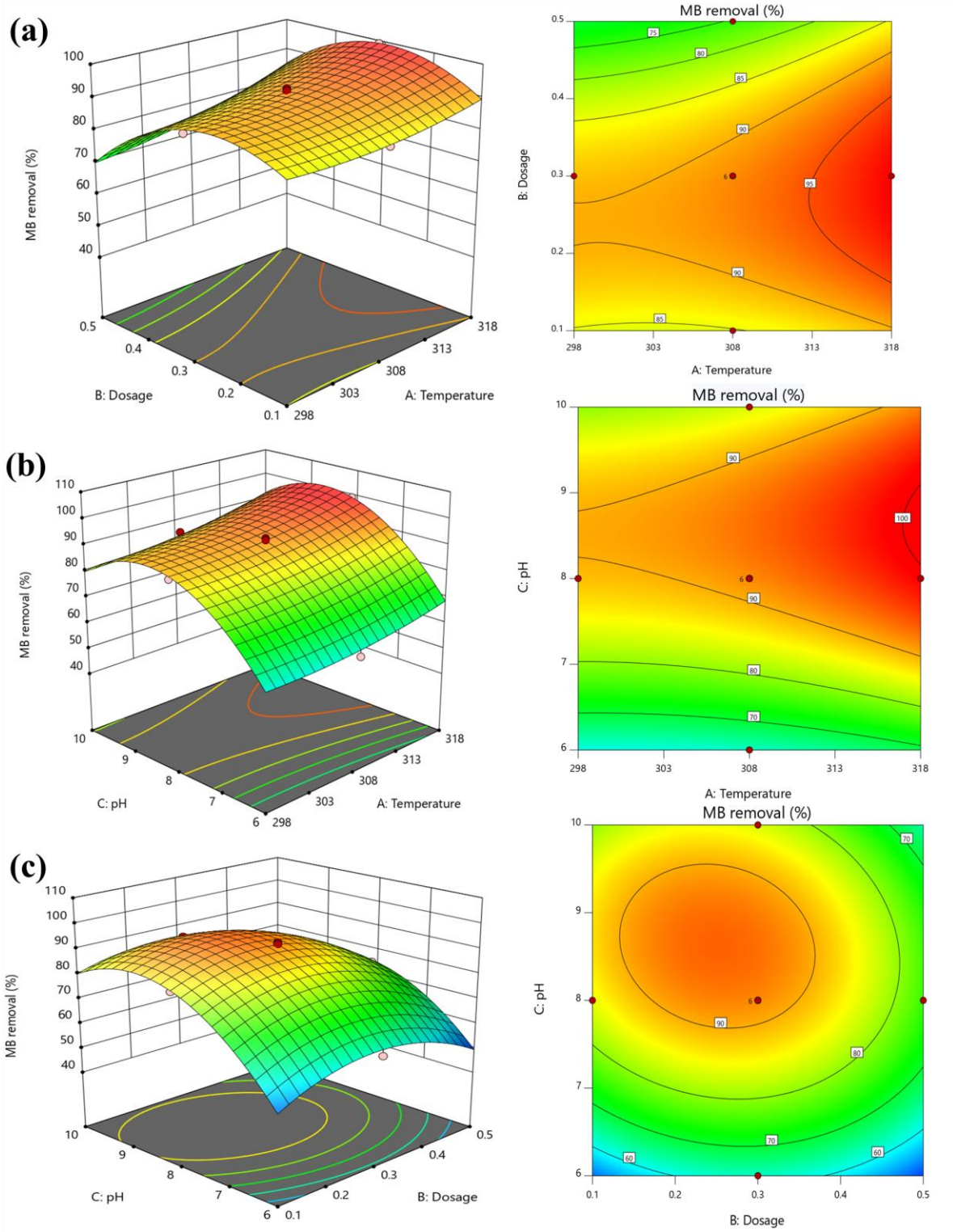

Fig. 8. 3-D response surface and 2-D contour plots for MB removal on GO@DSAC a function of (a) temperature and adsorbent dosage (b) temperature and pH and (c) adsorbent dosage and pH.

4. Conclusion

In this study, we employed cost-effective and fermented maize extract solution (MES) as a new cross-linker to enhance the adsorptive performance of a graphene oxide-based durian shell-derived activated carbon composite (GO@DSAC) for MB treatment. The MES facilitated the

gelatinization of the GO@DSAC composite, resulting in rapid precipitation without the production of byproducts. This demonstrates the benefits of easy separation, quicker preparation, and reduced GO loss. The as-synthesized GO@DSAC composite was fully characterized using techniques, including BET, FTIR, SEM/EDX, AFM, TEM, Zeta-potential, and XPS analysis. The SEM and BET examinations revealed that the composite material has a well-developed porous structure with an enhanced BET surface area of 803.67 m^2/g. The adsorption of MB was influenced by pH, initial concentration of MB, temperature, adsorbent dosage, contact time, and interfering ions. The adsorption kinetics and isotherms were well explained by the pseudo-second-order and Harkins-Jura models, respectively. The temperature-dependent thermodynamic parameters suggested that the adsorption process was spontaneous, feasible, and endothermic in nature. The adsorption process of MB on GO@DSAC involves both physical and chemical adsorption but more dominated by chemical rather than physical. Moreover, the regenerability and reusability studies revealed that the GO@DSAC composite could be effectively regenerated and reused for up to 10 consecutive cycles. The adsorption process demonstrated that the interaction between MB and GO@DSAC was governed by hydrogen bonding, pore-filling, and electrostatic attraction. The optimization study of the adsorption process using RSM-CCD revealed that the selected optimum conditions of temperature (316.17 K), adsorbent dosage (0.26 g/L), and pH (9.13) resulted in a maximum MB removal of 98.41%. This suggests that the developed composite could be employed in practical applications for the treatment of MB-containing wastewater.

References

Abd-Elhamid, A. I., Kamoun, E. A., El-Shanshory, A. A., Soliman, H. M. A., Aly, H. F., 2019. Evaluation of graphene oxide-activated carbon as effective composite adsorbent toward the removal of cationic dyes: Composite preparation, characterization and adsorption parameters, Journal of Molecular Liquids 279, 530–539.

Adel, M., Ahmed, M. A., Elabiad, M. A., Mohamed, A. A., 2022. Removal of heavy metals and dyes from wastewater using graphene oxide-based nanomaterials: A critical review, Environmental Nanotechnology, Monitoring & Management, 18, 100719.

Ahmad, R., Ejaz, M. O., 2023. Efficient adsorption of crystal violet (CV) dye onto benign chitosan-modified L-cysteine/bentonite (CS-Cys/Bent) bionanocomposite: Synthesis, characterization and experimental studies, Dyes and Pigments, 216, 111305

Ahmadian, M., Derakhshankhah, H., Jaymand, M., 2023. Biosorptive removal of organic dyes using natural gums-based materials: A comprehensive review, Journal of Industrial and Engineering Chemistry,

Albishri, W. S., Katouah, H. A., 2023. Functionalization of sodium magnesium silicate hydroxide/sodium magnesium silicate hydrate nanostructures by chitosan as a novel nanocomposite for efficient removal of methylene blue and crystal violet dyes from aqueous media, Arabian Journal of Chemistry, 16(7), 104804.

Al-Jubouri, M., Al-Jendeel, H. A., Rashid, S. A., Al-Batty, S., 2023. Green synthesis of porous carbon cross-linked Y zeolite nanocrystals material and its performance for adsorptive removal of a methyl violet dye from water, Microporous and Mesoporous Materials, 356, 112587.

Babakir, B. A. M., Ali, L. I. A., Ismail, H. K., 2022. Rapid removal of anionic organic dye from contaminated water using a poly(3-aminobenzoic acid/graphene oxide/cobalt ferrite) nanocomposite low-cost adsorbent via adsorption techniques, Arabian Journal of Chemistry, 15(12), 104318

Bhagat, S. K., Pilario, K. E., Babalola, O. E., Tiyasha, T., Yaqub, M., Onu, C. E., Pyrgaki, K., Falah, M. W., Jawad, A. H., Yaseen, D. A., Barka, N., Yaseen, Z. M., 2023. Comprehensive review on machine learning methodologies for modeling dye removal processes in wastewater, Journal of Cleaner Production, 385, 135522.

Boulahbal, M., Malouki, M. A., Canle, M., Redouane-Salah, Z., Devanesan, S., AlSalhi, M. S., Berkani, M., 2022. Removal of the industrial azo dye crystal violet using a natural clay: Characterization, kinetic modeling, and RSM optimization, Chemosphere, 306,135516.

Brandão, W. Q., Maciel, B. G., Lima, E. M. A., Mojica-Sánchez, L. C., da Silva, R. J., de Melo, C. P., 2023. Carboxymethylcellulose magnetic composite for adsorptive removal of cationic toluidine blue dye, Materials Chemistry and Physics, 303, 127782.

Cahyana, A. H., Liandi, A. R., Maghdalena, M., Yunarti, R. T., Wendari, T. P., 2022. Magnetically separable Fe_3O_4/graphene oxide nanocomposite: An efficient heterogenous catalyst for spirooxindole derivatives synthesis Ceramics International, 48 (13), 18316-18323.

Cao, D-X, Chen, Y., Jin, W-l, Li, W., Wang, R., Wang, K., Tang, A-a, Zhu, L-n., Kong, D-m., 2023. Non-porous covalent organic polymers enable ultrafast removal of cationic dyes via carbonyl/hydroxyl-synergetic electrostatic adsorption, Separation and Purification Technology, 315, 123689.

Chandra, T. C., Mirna, M. M., Sudaryanto, Y., Ismadji, S., 2007. Adsorption of basic dye onto activated carbon prepared from durian shell: Studies of adsorption equilibrium and kinetics, Chemical Engineering Journal, 127, 121-129.

Chandraraj, S. S., Xavier, J. R., 2023. Facile synthesis of graphene based mixed metal sulphide nanocomposite for energy storage applications, Surfaces and Interfaces, 36, 102515.

Chen, M., Yu, M., Kang, R., Sun, H., Zhang, W., Wang, S., Wang, N., Wang, J., 2022. Removal of Pb (II) and V (V) from aqueous solution by glutaraldehyde crosslinked chitosan and nanocomposites, Chemosphere 297, 134084.

David, P. S. Karunanithi, A., Fathima, N. N., 2020. Improved filtration for dye removal using keratin–polyamide blend nanofibrous membranes, Environmental Science and Pollution Research, 27, 45629-45638.

Demirezen, D. A., Yılmaz, D. D., Yıldız, Y. S., 2023. Magnetic chitosan/calcium alginate double-network hydrogel beads: Preparation, adsorption of anionic and cationic surfactants, and reuse in the removal of methylene blue, International Journal of Biological Macromolecules, 239, 124311.

Du, P., Zhang, J., Cai, Z., Ge, F., 2023. High adsorption of cationic dyes from aqueous solution using worm-like porous nanosilica: Isotherm, kinetics and thermodynamics, Materialstoday Communications, 35, 105697.

Elabboudi, M., Bensalah, J., Amri, A. E., Azzouzi, N. E., Srhir, B., lebkiri, A., Zarrouk, A., Rifi, E. H., 2023. Adsorption performance and mechanism of anionic MO dye by the adsorbent polymeric Amberlite®IRA-410 resin from environment wastewater: Equilibrium kinetic and thermodynamic studies, Journal of Molecular Structure, 1277,134789

Goswami, R., Dey, A. K., 2022. Synthesis and application of treated activated carbon for cationic dye removal from modelled aqueous solution, Arabian Journal of Chemistry, 15, 11, 104290.

Gul, A., Ma'amor, A., Khaligh, N. G., Julkapli, N. M., 2022. Recent advancements in the applications of activated carbon for the heavy metals and dyes removal, Chemical Engineering Research and Design,186, 276-299.

Han, X., Zhao, Y., Zhao, F., Wang, F., Tian, G., Liang, J., 2023. Novel synthesis of nanoscale zero-valent iron from iron ore tailings and green tea for the removal of methylene blue, Colloids and Surfaces A: Physicochemical and Engineering Aspects, 656, 130412.

Harraz, F. A., Rashed, M. A., Faisal, M., Alsaiari, M., Alsareii, S. A., 2022. Sensitive and selective electrochemical sensor for detecting 4-nitrophenole using novel gold nanoparticles/reduced graphene oxide/activated carbon nanocomposite, Colloids and Surfaces A: Physicochemical and Engineering Aspects, 654, 130068.

Hosseini, H., Zirakjou, A., McClements, D. J., Goodarzi, V., Chen, W-H., 2022. Removal of methylene blue from wastewater using ternary nanocomposite aerogel systems: Carboxymethyl cellulose grafted by polyacrylic acid and decorated with graphene oxide, Journal of Hazardous Materials, 421, 126752.

Hou, L., Zhang, X., Liu, H., Zheng, H., Niu, B., Zheng, J., Liu, S., Fu, J., 2023. Rigid-flexible coupled polyphosphazene supported polyurethane foam for efficient and selective adsorption of anionic dyes from water, Colloids and Surfaces A: Physicochemical and Engineering Aspects, 669, 131483.

Ihaddaden, S., Aberkane, D., Boukerroui, A., Robert, D., 2022. Removal of methylene blue (basic dye) by coagulation-flocculation with biomaterials (bentonite and *Opuntia ficus indica*), Journal of Water Process Engineering, 49, 102952.

Jasri, K., Abdulhameed, A. S., Jawad, A. H, ALOthman, Z. A., Yousef, T. A., Duaij, O. K. A., 2023. Mesoporous activated carbon produced from mixed wastes of oil palm frond and palm kernel shell using microwave radiation-assisted K_2CO_3 activation for methylene blue dye removal: Optimization by response surface methodology, Diamond and Related Materials, 131, 109581.

Jawad, A. H., Saber, S. E. M., Abdulhameed, A. S., Reghioua, A., ALOthman, Z. A., Wilson, L. D., 2022. Mesoporous activated carbon from mangosteen (*Garcinia mangostana*) peels by H_3PO_4 assisted microwave: Optimization, characterization, and adsorption

mechanism for methylene blue dye removal, Diamond and Related Materials, 129, 109389.

Jia, Z., Wu, L., Zhang, D., Han, C., Li, M., Wei, R., 2022. Adsorption behaviors of magnetic carbon derived from wood tar waste for removal of methylene blue dye, Diamond and Related Materials, 130, 109408

Jiang, M., Ma, Y., Wang, T., Niu, N., Chen, L., 2023. Hybrid lignin particles via ion-crosslinked for selective removal of anionic dyes from water, International Journal of Biological Macromolecules, 238, 124080.

Jing, Z., Li, Y., Zhang, Y., Chen, K., Sun, Y., Wang, M., Chen, B., Zhao, S., Jin, Y., Du, Q., Pi, X., Wang, Y., 2023. Simple synthesis of chitosan/alginate/graphene oxide/UiO-67 amphoteric aerogels: Characterization, adsorption mechanism and application for removal of cationic and anionic dyes from complex dye media, International Journal of Biological Macromolecules, 242, 124683.

Jing, Z., Li, Y., Zhang, Y., Wang, M., Sun, Y., Chen, K., Chen, W., Zhao, S., Jin, Y., Du, Q., Pi, X., Wang, Y., 2023. Enhanced methylene blue adsorption using zirconate alginate/graphene oxide/UiO-67 aerogel spheres: Synthesis, characterization, kinetic studies, and adsorption mechanisms, International Journal of Biological Macromolecules, 238, 124044.

Joshiba, G. J., Kumar, S., Rangasamy, G., Ngueagni, P. T., Pooja, G., Balji, G. B., Alagumalai, K., El-Serehy, H. A., 2022. Iron doped activated carbon for effective removal of tartrazine and methylene blue dye from the aquatic systems: Kinetics, isotherms, thermodynamics and desorption studies, Environmental Research, 215, 114317.

Karmakar, A., Paul, A., Santos, P. M. R., Santos, I. R. M., Guedes, da Silva, M. F. C., Pombeiro, A. J. L., 2023. Novel anthracene and pyrene containing Cd(II)-based coordination polymers for adsorptive removal of toxic dyes from aqueous medium, Colloids and Surfaces A: Physicochemical and Engineering Aspects, 670, 131488.

Kazak, O., Akkaya, G. K., Tor, A., 2023. Sustainable and efficient removal of cationic, anionic and neutral dyes from water by pre-deposited vinasse biochar membrane, Journal of Environmental Chemical Engineering, 11(3), 110042.

Konno, H., Tsukada, A., 2020. Size- and ion-selective adsorption of organic dyes from aqueous solutions using functionalized UiO-66 frameworks, Colloids and Surfaces A: Physicochemical and Engineering Aspects, 651, 129749.

Kumari, S., Khan, A. A., Chowdhury, A., Bhakta, A. K., Mekhalif, Z., Hussain, S., 2020. Efficient and highly selective adsorption of cationic dyes and removal of ciprofloxacin antibiotic by surface modified nickel sulfide nanomaterials: Kinetics, isotherm and adsorption mechanism, Colloids and Surfaces A: Physicochemical and Engineering Aspects, 586, 124264.

Li, J., Chen, Y., Zhou, T., Shi, H., Zheng, Z., Wang, Y., Guo, L., 2022. Dual-carbon coated $Na_3V_2(PO_4)_3$ derived from reduced graphene oxide and nanocellulose with porous structure for high performance sodium-ion batteries, Applied Surface Science,155553.

Li, R., Tang, X., Wu, J., Zhang, K., Zhang, Q., Wang, J., Zheng, J., Zheng, S., Fan, J., Zhang, W., Li, X., Cai, S., 2023. A sulfonate-functionalized covalent organic framework for record-high adsorption and effective separation of organic dyes, Chemical Engineering Journal, 464, 142706.

Lima, E. C., Hosseini-Bandegharaei, A., Moreno-Piraján, J. C., Anastopoulos, I., 2019. A critical review of the estimation of the thermodynamic parameters on adsorption equilibria. Wrong use of equilibrium constant in the Van't Hoof equation for calculation of thermodynamic parameters of adsorption, Journal of Molecular Liquids, 273, 425–434.

Liu, H., Tian, X., Xiang, X., Chen, S., 2022. Preparation of carboxymethyl cellulose/graphene composite aerogel beads and their adsorption for methylene blue, International Journal of Biological Macromolecules, 202, 632-643.

Liu, T., 2023. A natural armor-protected absorbent from discarded durian peel with rapid and recyclable absorption, high oil retention and self-cleaning ability, Colloids and Surfaces A: Physicochemical and Engineering Aspects, 666, 131294.

Mahmoud, M. E., Abdelwahab, M. S., Ibrahim, G. A. A., 2023. Surface functionalization of magnetic graphene oxide@bentonite with α-amylase enzyme as a novel bionanosorbent for effective removal of Rhodamine B and Auramine O dyes, Materials Chemistry and Physics, 301,127638.

Maimaiti, T., Hu, R., Yuan, H., Liang, C., Liu, F., Li, Q., Lan, S., Yu, B., Yang, S-T., 2022. Magnetic Fe_3O_4/TiO_2/graphene sponge for the adsorption of methylene blue in aqueous solution, Diamond and Related Materials, 123, 108811.

Meng, S., Nan, Z., 2022. Rapid and selective adsorption of organic dyes with ultrahigh adsorption capacity using Na and Fe co-doped g-C_3N_4, Separation and Purification Technology, 297, 121420.

Mirzaee, E., Sartaj, M., 2022. Activated carbon-based magnetic composite as an adsorbent for removal of polycyclic aromatic hydrocarbons from aqueous phase: Characterization, adsorption kinetics and isotherm studies, Journal of Hazardous Materials Advances, 6, 100083.

Moradi, O., Panahandeh, S., 2022. Fabrication of different adsorbents based on zirconium oxide, graphene oxide, and dextrin for removal of green malachite dye from aqueous solutions, Environmental Research, 214, 114042.

Mu, B., Xu, L., Yang, Y., 2023. Rational fabrication of completely amorphous chitosan-formyl-sucrose sorbents with excellent durability and regenerability for high-throughput dye removal, Chemical Engineering Journal, 461, 142134.

Mwizerwa, J. P., Liu, C., Xu, K., Zhao, N., Li, Y., Ndagijimana, P., Chen, Z., Shen, J., 2022. Activated carbon/reduced graphene oxide wrapped $LiFePO_4$ cathode for Li-ion batteries with ultrahigh capacities and high specific energy density, FlatChem, 34, 100393

Ndagijimana, P., Liu, X., Xu, Q., Lai, D., Wang, G., Pan, B., Wang, Y., 2021. Cassava flour extracts solution to induce gelatin cross-linked activated carbon-graphene oxide composites: The adsorption performance of dyes from aqueous media, Environmental Advances, 5, 100079.

Nouri, A., Ang, W. L., Mahmoudi, E., Chua, S. F., Mohammad, A. W., Benamor, A., Ba-Abbad, M. M., Leo, C. P., 2023. Decoration of polylactic acid on graphene oxide for efficient adsorption of methylene blue and tetracycline, Chemosphere, 322, 138219.

Obayomi, K. S., Lau, S. Y., Danquah, M. K., Zhang, J., Chiong, T., Meunier, L., Gray, S. R., Rahman, M. M., 2023a. Green Synthesis of Graphene-Oxide Based Nanocomposites for Efficient Removal of Methylene Blue Dye from Wastewater, Desalination, 564, 116749.

Obayomi, K. S., Lau, S. Y., Zahir, A., Meunier, L., Zhang, J., Dada, A. O., Rahman, M. M., 2023b. Removing methylene blue from water: A study of sorption effectiveness onto nanoparticles-doped activated carbon, Chemosphere, 313, 137533.

Obayomi, K. S., Lau, S. Y., Ibrahim, O., Jianhua, Z., Meunier, L., Maduakolam, A. M., Taiwo, A. B., Pramanik, B. K., Rahman, M. M., 2023c. Removal of Congo red dye from aqueous environment by zinc terephthalate metal organic framework decorated on silver nanoparticles-loaded biochar: mechanistic insights of adsorption, Microporous and Mesoporous Materials.

Obayomi, K. S., Lau, S. Y., Akubuo-Casmir, D., Yahya, M. D., Auta, M., A.S.M.F Bari, A. S. M. F., Oluwadiya, A. E., Obayomi, O. V., Rahman, M. M., 2022. Adsorption of endocrine disruptive congo red onto biosynthesized silver nanoparticles loaded on *Hildegardia barteri* activated carbon, Journal of Molecular Liquids, 352, 118735.

Pandey, D., Daverey, A., Dutta, K., Yata, V. K., Arunachalam, K., 2022. Valorization of waste pine needle biomass into biosorbents for the removal of methylene blue dye from water: Kinetics, equilibrium and thermodynamics study, Environmental Technology & Innovation, 25, 102200.

Pandey, D., Daverey, A., Dutta, K., Arunachalam, K., 2023. Dye removal from simulated and real textile effluent using laccase immobilized on pine needle biochar, Journal of Water Process Engineering, 53, 103710.

Rajendiran, R., Patchaiyappan, A., Harisingh, S., Balla, P., Paari, A., Ponnala, B., Perupogu, V., Lassi, U., Seelam, P. K., 2022. Synergistic effects of graphene oxide grafted chitosan & decorated MnO_2 nanorods composite materials application in efficient removal of toxic industrial dyes, Journal of Water Process Engineering, 47, 102704.

Rajesh, G., Senthil, P., Kumar, Akilandeswari, S., Rangasamy, G., Lohita, S., Uma, V., Shankar, Ramya, M., Nirmala, K., Thirumalai, K., 2023. Strategies for ameliorating the photodegradation efficiency of Mn-doped $CdAl_2O_4$ nanoparticles for the toxic dyes under visible light illumination, Chemosphere, 321, 138069.

Rather, R. A., Bhat, M. A., Shalla, A. H., 2023. Multicomponent interpenetrating metal-based Alginate-Carrageenan biopolymer hydrogel beads substantiated by graphene oxide for efficient removal of methylene blue from waste water, Chemical Engineering Research and Design, 182, 604-615.

Rimzim, Singh, J., Mittal, S., Singh, H., 2023. Robust removal of cationic dyes by zinc ferrite composites in single and ternary dye systems, Inorganic Chemistry Communications, 153, 110756.

Rostamian, M., Hosseini, H., Fakhri, V., Talouki, P. Y., Farahani, M., Gharehtzpeh, A. J., Goodarzi, V., Su, C-H., 2022. Introducing a bio sorbent for removal of methylene blue dye based on flexible poly(glycerol sebacate)/chitosan/graphene oxide ecofriendly nanocomposites, Chemosphere 289, 133219

Sadeghnezhad, M., Ghorbani, M., Nikzad, M., 2022. Synthesis of magnetic polypyrrole modified sodium alginate nanocomposite with excellent antibacterial properties and optimization of dye removal performance using RSM, Industrial Crops and Products, 189, 115192.

Saghir, S., Pu, C., Fu, E., Wang, Y., Xiao, Z., 2022. Synthesis of high surface area porous biochar obtained from pistachio shells for the efficient adsorption of organic dyes from polluted water, Surfaces and Interfaces, 34, 102357.

Saini, K., Sahoo, A., Kumar, J., Kumari, A., Pant, K. K., Bhatnagar, A., Bhaskar, T., 2023. Effective utilization of discarded reverse osmosis post-carbon for adsorption of dyes from wastewater, Environmental Research, 231, 116165.

Sajjad, M., Ahmad, F., Shah, A. L., Khan, M., 2022. Designing graphene oxide/silver nanoparticles-based nanocomposites by energy efficient green chemistry approach and their physicochemical characterization, Materials Science and Engineering B 284, 115899.

Serafin, J., Dziejarski, B., Junior, O. F. C., Sreńscek-Nazzal, J., 2023. Design of highly microporous activated carbons based on walnut shell biomass for H_2 and CO_2 storage Carbon, 201, 633-647.

Sharma, A. K., Dhiman, A., Nayak, A. K., Mishra, R., Agrawal, G., 2023. Environmentally benign approach for the efficient sequestration of methylene blue and coomassie brilliant blue using graphene oxide emended gelatin/κ-carrageenan hydrogels, International Journal of Biological Macromolecules, 219, 353-365.

Shimizu, T., De Silva, K. K. H., Hara, M., Yoshimura, M., 2022. Facile synthesis of carbon nanotubes and cellulose nanofiber incorporated graphene aerogels for selective organic dye adsorption, Applied Surface Science, 600, 154098

Singh, S., Naik, T. S. S. K., Anil, A. G., Khasnabis, S., Nath, B., Basavaraju, U, Kumar, V., Garg, V. K., Subramanian, S., Singh, J., Ramamurthy, P. C., 2022b. A novel CaO nanocomposite cross linked graphene oxide for Cr(VI) removal and sensing from wastewater, Chemosphere, 301, 134714.

Sinha, A. K., Sasmal, A. K., Pal, A., Pal, D., Pal. T., 2023. Ammonium phosphomolybdate $[(NH_4)_3PMo_{12}O_{40}]$ an inorganic ion exchanger for environmental application for purification of dye contaminant wastewater, Journal of Photochemistry and Photobiology A: Chemistry, 418, 113427.

Sun, L., Fang, K., Chen, W., Liu, K., Zhu, J., Zhang, C., 2022. Fabrication of a novel superhydrophobic cotton by HDTMS with TiO_2 supported activated carbon nanocomposites for photocatalysis and oil/water separation, Industrial Crops and Products, 189, 115836.

Sun, Y., Wang, T., Han, C., Lv, X., Bai, L., Sun, X., Zhang, P., 2022. Facile synthesis of Fe-modified lignin-based biochar for ultra-fast adsorption of methylene blue: Selective adsorption and mechanism studies, Bioresource Technology, 344, 126186.

Thakkar, H., Bhatt, M., Thakore, S., 2023. Barbituric acid derived covalent organic framework and its CNT composite as high-performance adsorbents for organic dye removal, Journal of Environmental Chemical Engineering, 11, 109890.

Thu, V. T., Trieu, M. H., An, N. H. T., Dat, N. T., Linh, N. D., Manh, N. B., 2023. Mussel – Inspired biosorbent combined with graphene oxide for removal of organic pollutants from aqueous solutions, Ecotoxicology and Environmental Safety, 255, 114793.

Tokula, B. E., Dada, A. O., Inyinbor, A. A., Obayomi, K. S., Bello, O. S., Pal, U., 2023. Agro-waste based adsorbents as sustainable materials for effective adsorption of Bisphenol A from the environment: A review, Journal of Cleaner Production, 388, 135819.

Wang, C., Fu, M., Cao, J., Wu, X., Hu, X., Dong, F., 2020. $BaWO_4$/g-C_3N_4 heterostructure with excellent bifunctional photocatalytic performance, Chemical Engineering Journal, 385, 123833.

Wang, F., Li, L., Iqbal, J., Yang, Z., Du, Y., 2022. Preparation of magnetic chitosan corn straw biochar and its application in adsorption of amaranth dye in aqueous solution, International Journal of Biological Macromolecules, 199, 234-242.

Wang, R., Cao, H., Yao, C., Peng, C., Qiu, J., Dou, K., Tsidaeva, N., Wang, W., 2023. Construction of alkalized MXene-supported $CoFe_2O_4$/CS composites with super-strong adsorption capacity to remove toxic dyes from aqueous solution, Applied Surface Science, 624, 157091.

Wang, C., Wang, Y., Shi, W-D., Yan, W-C., 2023. Electric field assisted assembly of nanoparticle loaded microspheres toward industrial applications for organic dye removal, Separation and Purification Technology, 306, 122565.

Wang, X., Qian, J., Chen, H., Li, X., Zhang, A., Li, X., Chen, C., He, Y., Xue, G., 2023. Achieving multi-cycle regeneration of activated carbon and Cr(VI) removal over a wide pH range by hydrothermal converting quinonimine dye into difunctional pyrrolic-N: Implication for carbon capture in printing and dyeing wastewater treatment, Chemical Engineering Journal, 459, 141646.

Xu, X. Zou, J., Teng, J., Liu, Q., Jiang, X-Y., Jiao, F-P., Yu, J-G., Chen, X-Q., 2018. Novel high-gluten flour physically cross-linked graphene oxide composites: Hydrothermal fabrication and adsorption properties for rare earth ions, Ecotoxicology and Environmental Safety, 166,1-10.

Xu, A., Gong, Y., Sun, Q., Li, L., Wang, F., Xiao, Z., Liu, R., 2023. Recoverable cellulose composite adsorbents for anionic/cationic dyes removal, International Journal of Biological Macromolecules, 238, 124022.

Xu, P., Shang, Z., Li, G., Sun, Y., He, K., Li, X., 2023. A novel silica-reinforced P(AM/AMPS/SA/TM-SiO_2) microspheres for selective adsorption of methylene blue from aqueous solution, Separation and Purification Technology, 313, 123495.

Yadav, S. K. Dhakate, S. R., Singh, B. P., 2022. Carbon nanotube incorporated eucalyptus derived activated carbon-based novel adsorbent for efficient removal of methylene blue and eosin yellow dyes, Bioresource Technology, 344, 126231.

Yan, Z., Qu, F., Liang, H., Yu, H., Pang, H., Rong, H., Van der Bruggen, B., 2021. Effect of biopolymers and humic substances on gypsum scaling and membrane wetting during membrane distillation, Journal of membrane Science, 617, 118638.

Yang, Z., Liu, X., Liu, X., Wu, J., Zhu, X., Bai, Z., Yu, Z., 2021. Preparation of β-cyclodextrin/graphene oxide and its adsorption properties for methylene blue, Colloids and Surfaces B: Biointerfaces, 200, 111605.

Yang, W., Cao, M., 2022. Study on the difference in adsorption performance of graphene oxide and carboxylated graphene oxide for Cu(II), Pb(II) respectively and mechanism analysis, Diamond and Related Materials, 129,109332.

Yu, M., Dong, H., Zheng, Y., Liu, W., 2021. Ternary metal oxide embedded carbon derived from metal organic frameworks for adsorption of methylene blue and acid red 73, Chemosphere, 280, 130567.

Zhang, X., Hou, l., Liu, H., Chang, l., Lv, s., Niu, B., Zheng, J., Liu, S., Fu, J., 2023. Hollow polyphosphazene microcapsule with rigid-flexible coupling cationic skeletons for highly efficient and selective adsorption of anionic dyes from water, Applied Surface Science, 626,157234.

Zhu, X., Zhou, G., He, G., Ma, L., Xu, B., Sun, F., 2023. Directly loading graphene oxide into melamine sponge for fast and high-efficiency adsorption of methylene blue, Surfaces and Interfaces, 36, 102575.